STARS

University of Central Florida
STARS

Electronic Theses and Dissertations, 2004-2019

2006

All-semiconductor High Power Mode-locked Laser System

Kyungbum Kim
University of Central Florida

Part of the Electromagnetics and Photonics Commons, and the Optics Commons

Find similar works at: https://stars.library.ucf.edu/etd

University of Central Florida Libraries http://library.ucf.edu

STARS Citation

Showcase of Text, Archives, Research & Scholarship

SYNCHRONIZATION IN ADVANCED OPTICAL COMMUNICATIONS

by

INWOONG KIM
B.S. Kyung Hee University, 1991
M.S. Korea Advanced Institute of Science and Technology, 1993

A dissertation submitted in partial fulfillment of the requirements
for the degree of Doctor of Philosophy
in the Department of Optics
in the College of Optics and Photonics
at the University of Central Florida
Orlando, Florida

Summer Term
2006

Major Professor: Guifang Li

ABSTRACT

All-optical synchronization and its application in advanced optical communications have been investigated in this dissertation. Dynamics of all-optical timing synchronization (clock recovery) using multi-section gain-coupled distributed-feedback (MS-GC DFB) lasers are discussed. A record speed of 180-GHz timing synchronization has been demonstrated using this device. An all-optical carrier synchronization (phase and polarization recovery) scheme from PSK (phase shift keying) data is proposed and demonstrated for the first time. As an application of all-optical synchronization, the characterization of advanced modulation formats using a linear optical sampling technique was studied. The full characterization of 10-Gb/s RZ-BPSK (return-to-zero binary PSK) data has been demonstrated.

Fast lockup and walk-off of the all-optical timing synchronization process on the order of nanoseconds were measured in both simulation and experiment. Phase stability of the recovered clock from a pseudo-random bit sequence signal can be achieved by limiting the detuning between the frequency of free-running self-pulsation and the input bit rate. The simulation results show that all-optical clock recovery using TS-DFB lasers can maintain a better than 5 % clock phase stability for large variations in power, bit rate and optical carrier frequency of the input data and therefore is suitable for applications in ultrafast optical packet switching.

All-optical timing synchronization of 180-Gb/s data streams has been demonstrated using a MS-GC DFB laser. The recovered clock has a jitter of less than 410 fs over a dynamic range of 7 dB.

All-optical carrier synchronization from phase modulated data utilizes a phase sensitive oscillator (PSO), which used a phase sensitive amplifier (PSA) as a gain block. Furthermore, all-

optical carrier synchronization from 10-Gb/s BPSK data was demonstrated in experiment. The PSA is configured as a nonlinear optical loop mirror (NOLM). A discrete linear system analysis was carried out to understand the stability of the PSO.

Complex envelope measurement using coherent linear optical sampling with mode-locked sources is investigated. It is shown that reliable measurement of the phase requires that one of the optical modes of the sampling pulses be locked to the optical carrier of the data signal to be measured. Carrier-envelope offset (CEO) is found to have a negligible effect on the measurement. Measurement errors of the intensity profile and phase depend on the pulsewidth and chirp of the sampling pulses as well as the detuning between the carrier frequencies of the data signal and the center frequency of the sampling source.

Characterization of the 10-Gb/s RZ-BPSK signal was demonstrated using the coherent detection technique. Measurements of the optical intensity profile, chirp and constellation diagram were demonstrated. A CW local oscillator was used and electrical sampling was performed using a sampling scope. A novel feedback scheme was used to stabilize homodyne detection.

ACKNOWLEDGMENTS

I would like to express my sincere thanks to my advisor Guifang Li, who guided me to achieve the final goal with confidence. I definitely thank to my co-advisor Patrick L. LiKamWa. He taught me how beautiful time this period would be.

I appreciate helpful discussions with my former group member Dr. Cheolhwan Kim. I also thank to Daniel May-Arrioja and Hyungseok Bang who shared valuable times in the laboratory and the office. I would like to express thanks to Gilad Goldfarb, Kevin Croussore, and Xiaoxu Li for valuable discussions in the group. I thank to Kevin Croussore, Ivan Carlos Vivanco, and Nathan Bickel for their kind help in my thesis work.

Finally, and most importantly, my sincere acknowledgements go to my wife, Namju Bang, who has supported for this journey of study. I have been able to enjoy studying and researching while I was able to have lovely time with my wife and son. I express my gratitude to my family in Korea who has encouraged me in challenging this expedition all the time.

TABLE OF CONTENTS

LIST OF FIGURES

LIST OF TABLES

LIST OF ACRONYMS/ABBREVIATIONS

ASE   Amplified spontaneous emission

Bi-NLF   Bismuth-oxide-based nonlinear fiber

BPSK   Binary phase shift keying

CEO   Carrier-envelope offset

CSRZ   Carrier-suppressed return-to-zero

CW   Continuous wave

DD-PLL   Decision-driven phase lock loop

DFWM   Degenerate four-wave mixing

DPSK   Differential phase shift keying

DSP   Digital signal processing

DWDM   Dense wavelength division multiplexing

EDFA   Erbium-doped fiber amplifier

FBG   Fiber Bragg gratings

fs   Femtosecond ($=10^{-12}$ s)

FWHM   Full width at half maximum

FWM   Four-wave mixing

Gb/s   Giga bit per second (Giga = 10^{9})

GHz   Gigahertz ($=10^{9}$ Hz)

HNLF   Highly nonlinear fiber

MS-GC DFB   Multi-section gain-coupled distributed feedback

NDFWM   Non-degenerate four-wave mixing

NMZI	Nonlinear Mach-Zehnder interferometer
NOLM	Nonlinear optical loop mirror
NRZ-BPSK	Non-return-to-zero Binary phase shift keying
ns	Nanosecond (=10^{-9} s)
OOK	On-off keying
OPO	Optical parametric oscillator
OTDM	Optical time-division multiplexing
PI	Proportional-integral
PLL	Phase-locked loops
PRBS	Pseudo-random binary sequence
PSA	Phase sensitive amplifier
PSK	Phase shift keying
PSO	Phase-sensitive oscillator
QPSK	Quadrature phase shift keying
RF	Radio-frequency
RMS	Root-mean-square
RZ-BPSK	Return-to-zero binary phase shift keying
RZ-DPSK	Return-to-zero differential phase shift keying
RZ-DQPSK	Return-to-zero differential quadrature phase shift keying
SNR	Signal-to-noise ratio
SSMF	Standard single-mode fiber
TS-DFB	Two-section distributed feedback
TS-GC DFB	Two-section gain-coupled distributed feedback

WDM   Wavelength division multiplexing

CHAPTER 1: INTRODUCTION

1.1 Review

Fiber-optic communication systems have contributed to the massive growth of the telecommunication industry since the mid-seventies, making it possible to meet the increasing demand for communication services in terms of quantity and quality. Even with the down turn in the optical communication market around the year 2000, digital communication traffic has continued to expand rapidly in the past six years. New service concepts with better quality of information are emerging constantly. It is this demand that has driven the evolution of optical communication technologies.

One approach to expanding transmission capacity is increasing the bit rate beyond 40 Gb/s in a single channel using optical time-division multiplexing (OTDM). 160-Gb/s data transmission over 275.4 km of standard single-mode fiber (SSMF) was demonstrated using OTDM in 2004 [1]. 320-Gb/s single-polarization OTDM transmission over 80 km of SSMF was demonstrated in 2005 [2].

Clock recovery (timing synchronization) is very important in digital communication since all digital data are recovered based on a recovered clock. To avoid using an additional channel for the clock signal, we can recover it from the incoming data at the receiver site. All-optical timing synchronization becomes an efficient way of timing synchronization when the data rate is above 100 GHz [3, 4].

The other approach to expanding transmission capacity is to increase the spectral efficiency using advanced modulation formats to decrease the cost per bit while increasing the transmission capacity. 2-b/s/Hz 40-Gb/s dense wavelength division multiplexing (DWDM) transmission over

400 km of SSMF was demonstrated using RZ-DQPSK (return-to-zero differential quadrature phase shift keying) [5]. wavelength division multiplexing (WDM) transmission using RZ-differential 8-level PSK over 320 km of SSMF was demonstrated [6].

In the future, combining these two techniques will be a reasonable means to boost traffic capacity. Increasing spectral efficiency using advanced modulation format with high symbol rate can also reduce the number of wavelength channels to be managed in long-haul networks. Recently, a single-channel 640-Gb/s DQPSK transmission over 480-km of SSMF was demonstrated [7]. The symbol rate was 160 Gs/s using OTDM in each polarization, and the spectral efficiency was increased by multilevel modulation and polarization multiplexing.

In parallel with efforts to increase transmission, all-optical regeneration has been investigated to overcome transmission impairments caused by the combined effects of noise accumulation, fiber dispersion, fiber nonlinearities, and inter-channel crosstalk. These effects can lead to amplitude noise, jitter and phase noise. All-optical regeneration is potentially ultrafast, thereby avoiding any possible electronic bottle-neck. High speed all-optical regeneration of OOK (on-off keying) has been demonstrated by many research groups [8]. Recently, all-optical regeneration of RZ-DPSK was demonstrated [9, 10].

In coherent communication, homodyne detection has better sensitivity than heterodyne detection. To take advantage of advanced modulation formats and homodyne detection, digital signal processing (DSP) enabled coherent detection has been recently demonstrated [11]. A continuous wave (CW) local oscillator was used without phase locking loop. The carrier phase was estimated in post processing for data recovery. A spectral efficiency of 2.5-b/s/Hz was demonstrated in WDM transmission of polarization-multiplexed 40-Gb/s QPSK signals with 16-

GHz spacing [11]. This demonstration showed that DSP enabled coherent homodyne demodulation has better sensitivity than that of differential demodulation.

Recently linear optical sampling, based on coherent detection, has been studied for characterization of advanced modulation formats in optical communication. It can not only resolve pulse profiles with high temporal resolution because of narrow optical sampling pulsewidth but also measure optical phase profiles because of phase sensitive coherent detection. The measurement of the eye diagram at 640 Gb/s was demonstrated [12]. The complete characterization of optical data at 40 Gb/s (pulse profile and frequency chirp or phase profile) was presented in [13]. Furthermore, the measurement of constellation diagram on the 40-Gb/s BPSK (binary PSK) was demonstrated [14].

Carrier phase and polarization recovery (carrier synchronization) is very important for coherent detection since it is based on optical interference. Both the optical phase and the polarization of the local oscillator carrier should be locked with respect to those of the optical data. Carrier synchronization is also required for all-optical regeneration of DPSK, since it uses a phase sensitive amplifier (PSA). The PSA is based on non-degenerate four-wave mixing, whose process is sensitive to the carrier phase and polarization, in nonlinear optical loop mirror (NOLM) [9].

As the bit (or symbol) rate increases in future optical communication systems, synchronization of clock and optical carrier is becoming an issue. The details of synchronizations are discussed in the following section.

Optical On-Off Keying

Fig. 1.1. Timing synchronization and its applications

Optical Phase-Shift Keying
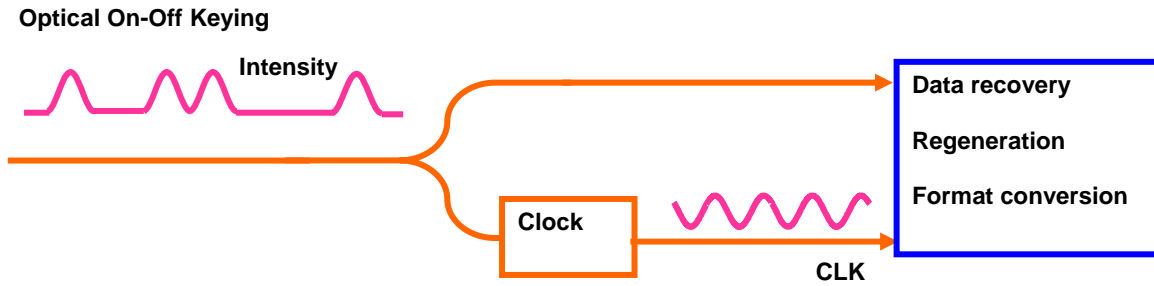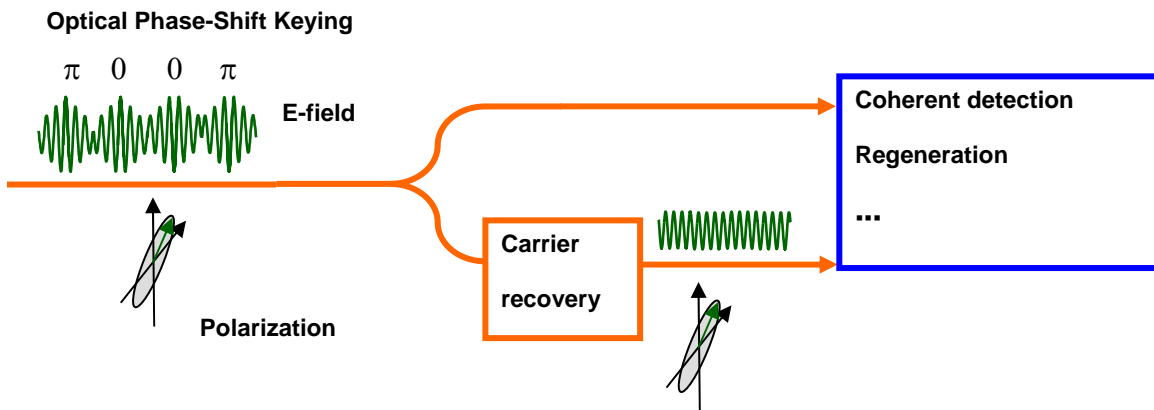
Fig. 1.2. Carrier synchronization and its applications

1.2 Synchronization

1.2.1 Timing synchronization

Fig. 1.1 shows the schematic diagram of clock recovery (timing synchronization) and its applications. A clock signal is recovered from intensity modulated data. The recovered clock can be used for data recovery, regeneration, format conversion and so on [3, 8, 15, 16]. The quality of the timing synchronization in terms of amplitude and phase noise determines the performance of the system.

Various high-speed electrical [17, 18], optical [3, 15, 19-24], and hybrid [25, 26] timing synchronization techniques have been studied. All-optical timing synchronization techniques can operate at ultrafast speeds above 100 GHz, thus overcoming the limit set by electronics.

Two-section distributed feedback lasers (TS-DFB) have been a most promising candidate for all-optical timing synchronization for the following reasons. The self-pulsation of TS-DFB lasers can be easily tuned from tens of GHz to hundreds of GHz by controlling injection currents [27-30]. The locking time of clock recovery (timing synchronization) is ultrafast (< 1 ns). The device is very compact and low cost [31].

1.2.2 Phase and polarization Synchronization

Fig. 1.2 shows the schematic diagram of carrier phase and polarization recovery (carrier synchronization) and its applications. Optical carrier phase and polarization are recovered from phase modulated data. The recovered carrier can be used for coherent detection, regeneration and so on [9, 11, 32]. Advanced modulation formats that utilize PSK (phase shift keying) tend to

suppress the carrier which prohibits use of injection locking for carrier synchronization. There have been demonstrations of decision-driven phase lock loop (DD-PLL) [32, 33], but wide locking bandwidth is hard to achieve for practical purposes. Recently, digital feed-forward techniques have been proposed and demonstrated [11, 34], however both techniques require polarization alignment/diversity. Polarization tracking/diversity adds to system complexity and cost. In addition, optical regeneration of coherent modulation formats such as PSK requires a local oscillator locked to the phase and polarization of the data signal.

1.2.3 Characterization of data and synchronizations

The electronic sampling scope is limited to about 100 GHz of bandwidth. Optical sampling techniques can overcome the limit of electronic sampling. Temporal resolution of optical sampling is limited by the sampling pulsewidth. There are two major optical sampling techniques [12, 35]. One is nonlinear optical sampling and the other is linear optical sampling. Fig. 1.3(a) shows the schematic diagram of nonlinear optical sampling. The optical sampling pulse, with short pulsewidth, interacts with the intensity modulated optical data in a nonlinear optical media to generate a new optical frequency. This nonlinear optical process combined with short sampling pulses works as a sampling gate. The new optical frequency components, proportional to the optical intensity of data at sampling time, is filtered and measured. It has low conversion efficiency because it uses second-order or third-order nonlinearity [12].

6
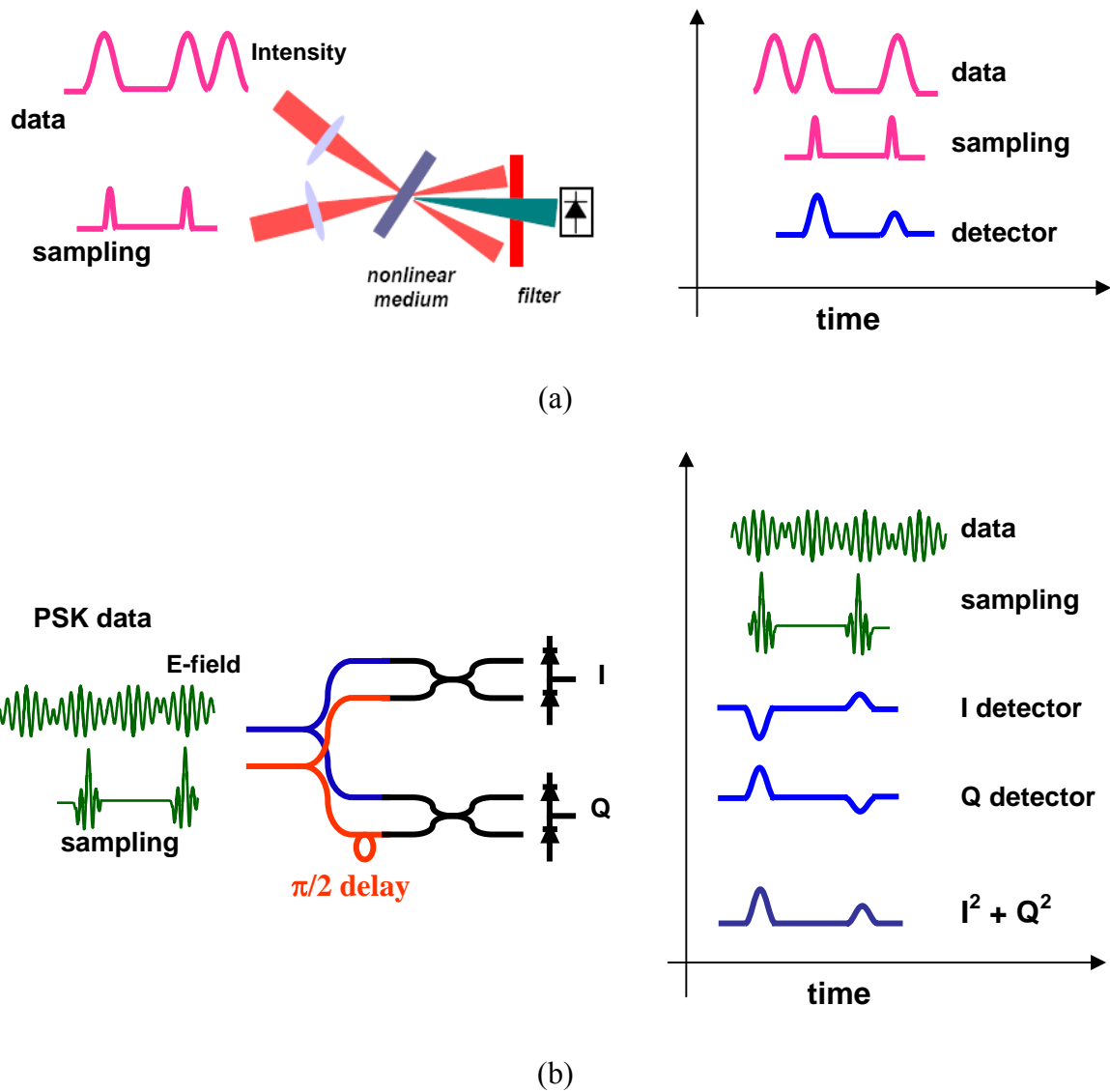
Fig. 1.3. Schematic diagrams of optical samplings and time domain signals. (a) nonlinear optical sampling, (b) linear optical sampling.

Fig 1.3(b) shows the schematic diagram of linear optical sampling based on coherent detection. The sampling pulse works as a gate, too. When there is no sampling pulse, the signals from the balanced detectors are zero. The signals from the balanced detectors depend on the intensities and phases of data because of interference between the sampling pulses and the data. Linear optical sampling uses a 90° optical hybrid to measure the in-phase (I) and quadrature-

phase (Q) signal. Sum of squared signal from I and Q channels is proportional to the intensity of data. This provides better sensitivity compared to nonlinear optical sampling [12]. In addition, we can measure the phase of data since the signal from I and Q detectors are phase sensitive. The sum of the square signals from I and Q detectors are proportional to the intensity of data. The ability to measure intensity and phase makes it appropriate for the characterization of data utilizing advanced modulation formats. Because linear optical sampling is based on coherent detection, carrier phase and polarization have to be synchronized along with timing for sampling.

1.3 Statement of dissertation

The objective of this work is to study all-optical timing synchronization and all-optical carrier synchronization. Full characterization of data utilizing advanced modulation format requires measuring the intensity profile and phase profile at the same time using coherent detection. The measurement requires timing synchronization and carrier synchronization. The work is divided into three parts.

1) All-optical timing synchronization

a) The dynamics of all-optical timing synchronization using TS-DFB (two-section DFB) lasers has not been studied systematically. The numerical simulation and experimental results were compared and analyzed to understand lockup time (defined as the time required for the self-pulsation frequency of the TS-DFB laser to be locked to the bit rate of the injected data) and walk-off time (defined as the time it takes for the injection-locked TS-DFB laser to relax to its free-running state) of the clock-recovery. Study on dynamics provides key ideas to get a high

quality of recovered clock with low phase noise against pattern effect, power drift, bit-rate drift and wavelength drift. It was found that phase stability of recovered clock can be achieved by limiting the detuning between the frequency of free-running self-pulsation and the input bit rate.

b) The limit of the all-optical timing synchronization was studied using multi-section gain-coupled DFB (MS-GC DFB) lasers. MS-GC DFB lasers showed more than 230-GHz tuning range of self-pulsation frequency [29]. For comparison, TS-GC DFB laser has about 120 GHz of tuning range [30]. The world record of 180-GHz timing synchronization at the aggregate line rate was demonstrated. This achievement shows the possibility of the application for ultrafast timing synchronization for future optical communications.

2) All-optical carrier synchronization

Prior to this research no method has been proposed for all-optical carrier synchronization. The method proposed here can recover the optical carrier phase and polarization as well. The scheme uses a phase-sensitive optical oscillator, which has a phase sensitive amplifier as a gain block. The first demonstration of all-optical carrier synchronization was demonstrated from a 10-Gb/s BPSK (binary phase-shift keying) signal.

3) Characterization of optical data

a) Requirements for the sampling source in coherent linear sampling have been studied. The effects of sampling pulsewidth, chirp, and carrier frequency (with respect to the carrier frequency of data) have been studied theoretically. It was reported that carrier-envelope offset (CEO) was

contributing to the deterministic rotation of measured phase [36]. However, it was found that the frequency difference between data carrier and sampling carrier determines the deterministic phase error.

b) The characterization of 10-Gb/s BPSK data was performed using a CW local oscillator. The constellation diagram (intensity and phase of sampled data on complex plane), intensity profile and chirp profile has been measured. The transmission laser was split to be used as a CW local oscillator for coherent homodyne detection. A new stabilization method was used for homodyne detection. The stabilization method does not require pilot tone (leaving optical carrier tone by incomplete BPSK modulation) [37], dithering signal (adding phase modulation at a specific frequency) [38], or DD-PLL [33]. The measurement technique was demonstrated even after transmission of 6 km of HNLF (highly nonlinear fiber), which enabled to observe the development of chirp of data.

1.4 Outline of dissertation

Chapter 1 is the introduction. Chapter 2 describes ultrafast all-optical timing synchronization (clock recovery) in multi-section DFB lasers. The first part is a study on dynamics and the second part is the experiment for 180 GHz all-optical timing synchronization. Chapter 3 presents all-optical carrier phase and polarization synchronization (carrier recovery). The phase sensitive oscillator is studied and the experimental demonstration is given. Chapter 4 discusses requirements for the sampling source in coherent linear sampling. In the experiment,

characterization of optical data using a CW local oscillator is presented. Chapter 5 is the summary and future of the work.

CHAPTER 2: TIMING SYNCHRONIZATION

2.1 Introduction

All-optical clock recovery (timing synchronization) using two-section distributed feedback (TS-DFB) lasers have been studied extensively [3, 15, 19-22]. Two-section gain (or loss) coupled DFB lasers have been shown to produce self-pulsation signals with a higher modulation index than index-coupled DFB lasers [39]. The advantages of all-optical timing synchronization using TS-DFB lasers include high-speed operation above tens of gigahertz, wide tuning range of data rates up to hundreds of gigahertz, compactness, and wide locking bandwidth.

There are two schemes of operation for all-optical timing synchronization using two-section DFB (TS-DFB) lasers [3]. The first scheme is the so-called incoherent clock recovery (timing synchronization) which is characterized by the following: 1) Injection data is carried on a wavelength that is at least 1 nm detuned from that of the free-running TS-DFB laser, and 2) Injection power is typically larger than 1 mW. The mechanism of this method is as follows. The injection signal creates carrier modulation at the clock frequency in the front section of the TS-DFB laser. This carrier modulation creates sidebands situated at the clock frequency on either side of the laser mode of the front section. Owing to optical coupling between the two sections, one of the resulting sidebands injection locks the laser mode of the back section. Beating of the two modes results in the recovered clock. The advantages of this scheme are 1) it is wavelength insensitive as the timing synchronization mechanism depends on intensity-induced carrier modulations, and 2) it can be potentially polarization insensitive if the gain region of the laser is properly strained. The disadvantages of this scheme are 1) it requires relatively high injection

power, i.e., the sensitivity of timing synchronization is low, and 2) jitter of the recovered clock is relatively high.

The second scheme is the so-called coherent clock recovery (timing synchronization) whose circuitry is characterized by the following: 1) Injection data is carried on almost the same wavelength as that of the free-running TS-DFB laser, and 2) Injection power is less than $10\ \mu W$. The mechanism is as follows. The injection signal contains sidebands due to existence of the clock component in its optical spectrum. One of the sidebands is aligned with the laser mode of the front section and the optical carrier is aligned with the laser mode of the back section. Optical injection locking takes place in both sections. Beating of the two optically injection-locked modes results in the recovered clock. The advantages of this scheme are 1) it requires extremely low injection power, i.e., the sensitivity of timing synchronization is high, and 2) the jitter of the recovered clock is very small. The disadvantages of this scheme are 1) it is wavelength sensitive, and 2) it is polarization sensitive even if the gain region is properly strained.

Through wavelength and polarization insensitive wavelength conversion, all-optical coherent timing synchronization can become wavelength and polarization insensitive (Fig. 2.1) [20, 23]. Optical carrier and clock components of the injected data signal carried on arbitrary wavelength (λ_L) and polarization are first converted onto the probe wavelength (λ_o) and polarization, which are matched with the laser modes of the free-running TS-DFB laser. This makes the coherent timing synchronization insensitive to both wavelength and polarization of the injection signal. The polarization insensitive all-optical wavelength conversion can be achieved above 160 Gb/s in principle [40]. Because of the benefit of coherent timing synchronization, the simulation and experimental works were focused on this operation scheme.
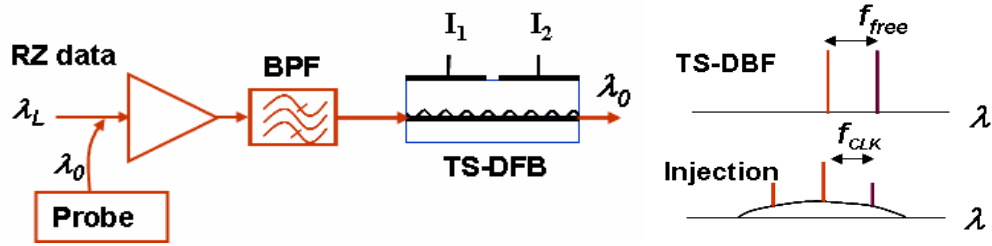
Fig. 2.1. Schematic diagram of wavelength and polarization insensitive coherent timing synchronization. BPF: band pass filter, I_1 and I_2: injection currents, f_{CLK}: clock frequency, f_{free}: free-running self-pulsation frequency.

Section 2.2 studies dynamics of all-optical timing synchronization in TS-DFB lasers. 180-GHz all-optical timing synchronization using multi-section gain-coupled DFB (MS-GC DFB) lasers is presented in section 2.3.

2.2 Dynamics of all-optical timing synchronization using two-section distributed feedback (TS-DFB) lasers

2.2.1 Introduction

Reported studies on all-optical timing synchronization using TS-DFB lasers have mostly concentrated static properties such as tuning range of self-pulsation, locking bandwidth, operation scheme and so on. It is important to understand the dynamic properties of all-optical timing synchronization using TS-DFB lasers such as lockup time (defined as the time required for the self-pulsation frequency of the TS-DFB laser to be locked to the bit rate of the injected data), walk-off time (defined as the time it takes for the injection-locked TS-DFB laser to relax

to its free-running state), and stability of the phase relationship between the recovered clock and input data, which are especially crucial for applications in optical packet switching. The lockup time affects system latency [3]. Long walk-off time of the recovered clock is important to maintain the phase of the recovered clock with respect to data signals of different patterns. Lockup time on the order of sub-nanosecond and walk-off time of a few nanoseconds have been reported experimentally using both two-section index- and gain-coupled DFB lasers [3, 22]. The asymmetry in lockup time and walk-off time of clock recovery (timing synchronization) using TS-DFB lasers, however, has not been explained so far. In addition, the dynamic evolution of the clock phase in the walk-off period and the phase stability (timing jitter) of the recovered clock under different patterns of the input data has not been studied systematically.

$$z = -l_a \qquad z = 0 \qquad z = l_b$$

injection

F_a $\rightarrow$	F_b $\rightarrow$
B_a $\leftarrow$	B_b $\leftarrow$
Section a	Section b

r_1 r_2
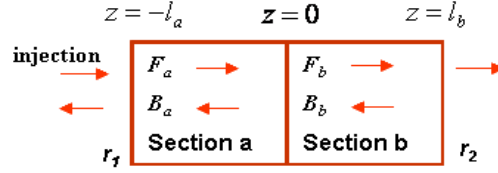
Fig. 2.2. Schematic diagram of a TS-DFB laser for numerical modeling

The simulation and experimental study show the dynamics of lockup and walk-off as well as phase dynamics of the recovered clock under PRBS (pseudo-random binary sequence) data injection. Based on the excellent agreement in the deterministic timing synchronization behaviors between the experiments and simulation, we extend our simulation to predict the phase difference between the recovered clock and the input data under different injection conditions (bit rate, wavelength, and input power) and different device parameters. It is shown that less than 5 % phase error can be maintained over a wide range of conditions suggesting that the TS-

15

DFB laser can be used for ultrafast variable bit-rate timing synchronization for applications in optical packet switching [3].

2.2.2 Numerical model

A large-signal spatiotemporal finite-difference method was used to investigate the dynamics of coherent timing synchronization in TS-DFB lasers [39, 41]. A TS-DFB laser has two sections as shown on the figures. Section a (front section) extends from $z = -l_a$ to $z = 0$; section b (back section) extends from $z = 0$ to $z = l_b$. The spatiotemporal dynamics of the TS-DFB laser are completely characterized by the carrier number density, N_s, and the electric field $E_s(z,t) = F_s(z,t)\exp[-i(\omega t - \beta z)] + B_s(z,t)\exp[-i(\omega t + \beta z)]$, where F_s and B_s represent the slowly-varying envelopes of the forward and backward waves which are coupled through the DFB structure.

The rate equation of the carrier density and the coupled-mode equations of the slowly-varying envelopes are given by

$$\frac{\partial N_s(z,t)}{\partial t} = \frac{I_s}{qV_s} - \frac{N_s(z,t)}{\tau_s} - \frac{g_{ns}\left(N_s(z,t) - N_{0s}\right)}{1 + \varepsilon_s P_s(z,t)} v_s P_s(z,t)$$

$$\frac{\partial F_s(z,t)}{\partial z} + \frac{1}{v_s}\frac{\partial F_s(z,t)}{\partial t} = \frac{1}{2}[G_s(N_s(z,t)) - \Gamma_s]F_s(z,t) + i\kappa_s B_s(z,t) \qquad (2.1)$$

$$\frac{\partial B_s(z,t)}{\partial z} - \frac{1}{v_s}\frac{\partial B_s(z,t)}{\partial t} = -\frac{1}{2}[G_s(N_s(z,t)) - \Gamma_s]B_s(z,t) - i\kappa_s F_s(z,t),$$

where the subscript s is a or b denoting each section, q is the electron charge, and κ_s is the complex coupling coefficient of the DFB section. If κ_s is real (imaginary), the DFB laser is a purely index- (gain- or loss-) coupled. Spontaneous emission noise that leads to a finite coherence time for the free-running self-pulsation signal was ignored in the simulation.

The gain coefficient $G_s(N_s)$ is given by

$$G_s\left(N_s(z,t)\right) = g_{ns}\left(N_s(z,t) - N_{0s}\right)\left[\frac{1}{1+\varepsilon_s P_s(z,t)} - i\alpha_s\right] + i\Delta\beta_s, \qquad (2.2)$$

where α_s is the linewidth enhancement factor and $P_s = |F_s|^2 + |B_s|^2$ is the photon density.

The detuning from Bragg condition $\Delta\beta_s$ is given by

$$\Delta\beta_s = \Delta\beta_{cs} + \frac{\delta\beta}{\delta I}I_s$$

$$\Delta\beta_{cs} = \beta_s - \frac{\pi}{\Lambda_s} = \frac{2\pi n_{eff,s}}{\lambda} - \frac{\pi}{\Lambda_s} \qquad , \qquad (2.3)$$

where $\delta\beta(\mathrm{cm})/\delta I(\mathrm{mA})$ is the current-dependent thermal tuning (set to 1.0 according to the experimental result reported on the literature [42]), $n_{eff,s}$ is the effective index, and Λ_s is the period of the corrugation. A static detuning $\Delta\beta = \Delta\beta_a - \Delta\beta_b$ between the two sections is introduced in this simulation representing DFB structures with different corrugation periods or different effective indices between two sections.

The boundary conditions that complete the partial differential Eq. (2.1) are given by

$$F_a(-l_a,t)exp(-i\beta_a l_a) = r_1 B_a(-l_a,t)exp(i\beta_a l_a) + t_1 S_{inj}(t)$$

$$B_b(l_b,t)exp(-i\beta_b l_b) = r_2 F_b(l_b,t)exp(i\beta_b l_b) \ ,$$

(2.4)

where r_1 and r_2 are the reflection coefficients of the electric field on the left and right facets of the laser respectively, and t_1 is the transmission coefficient on the left facet. The injected data signal was added as a boundary condition for the simulation of the coherent timing synchronization process [43]. The injected data signal $S_{inj}(t)$ fed through the left facet is given by

$$S_{inj}(t) = A_{inj}d(t)(e^{-i\Omega_1 t} + e^{-i\Omega_2 t}) \ ,$$

(2.5)

which is of the carrier-suppressed return-to-zero (CSRZ) format [16, 44]. The CSRZ format is chosen for its simplicity in both simulation and experiment. The results presented here apply to other return-to-zero formats. In Eq. (2.5), A_{inj} is the amplitude of the injection field, $d(t) = 1(or\,0)$ is data value, Ω_1 and Ω_2 are the angular frequencies (measured from Bragg condition) of the clock components contained in the injected data signal. The bit rate of the input data B_{inj} is given by $|\Omega_2 - \Omega_1|/(2\pi)$. The laser modes of the self-pulsing TS-DFB laser should be close to the clock components in the injected data signal and the injection power should be high enough to lock the modes of the TS-DFB laser [3, 45-48].

2.2.3 Experimental Setup

The experimental setup is shown in Fig. 2.3. A carrier-suppressed return-to-zero (CSRZ) data at 24-G/s was generated using a tunable laser and two cascaded LiNbO$_3$ modulators. The first modulator was modulated by a 12-Gb/s NRZ data from a pattern generator. Edited word patterns as well as PRBS were used for the NRZ data. The second modulator was biased at the null and modulated by the 12-GHz 2-V_π peak-to-peak amplitude clock signal from the pattern generator. As a result, the optical data signal was the CSRZ format consisting of 24-Gb/s 2-bit words.

The CSRZ data was injected into the TS-DFB laser through a polarization controller and a circulator. The output signal from the TS-DFB laser was optically amplified, converted into the electrical signal using a high speed photodetector, and analyzed in time domain using a digital sampling oscilloscope or in frequency domain using a RF spectrum analyzer to measure the frequency of the recovered clock. In addition, the phase of the recovered clock was directly measured by mixing the recovered clock with the clock signal from the pattern generator in a harmonic mixer.
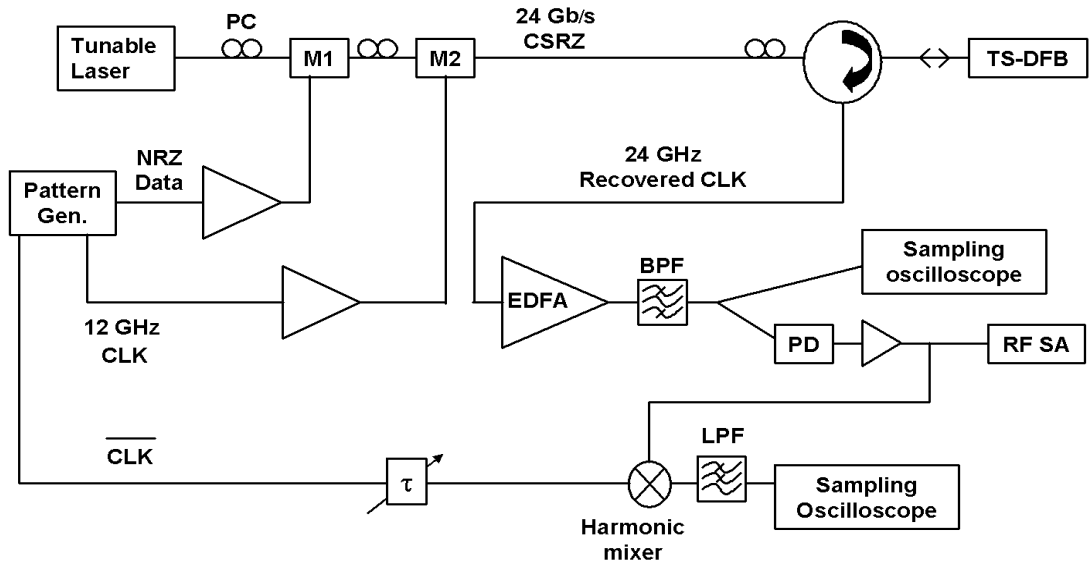
Fig. 2.3. Schematic of the experimental setup. M1 and M2: modulators, PC: polarization controller, RF SA: RF spectrum analyzer, PD: photodetector, τ : delay.

Table 2.1. Simulation parameters for TS-DFB lasers

	Partially gain-coupled		Index-coupled
Self-pulsation frequency (f_{free}, GHz)	23.9	39.9	39.85
Coupling coefficient (κ_s, cm^{-1})	140+14$\boldsymbol{i}$		113
Volume ($V_a = V_b$, cm^3)	141.75 x 10^{-12}		
Length ($l_a = l_b$, cm)	0.035		
Differential gain (g_s, cm^2)	1.6 x 10^{-16}		
Carrier lifetime (τ_s, s)	1.25 x 10^{-9}		
Transparent carrier density (N_{0s}, /cm^3)	2.1 x 10^{18}		
Group velocity (v_s, cm/s)	3 x 10^{10} / 3.7		
Effective index ($n_{eff,s}$)	3.55		
Linewidth-enhancement factor (α_s)	-3		
Loss coefficient ($\varGamma_s$, cm^{-1})	40		
Facet reflectivity (r_s)	1 x 10^{-6}		
Gain suppression factor (ε_s, cm^3)	3 x 10^{-17}		
Bragg detuning ($\Delta\beta_{ca}$, cm^{-1})	15	20.34	0
Bragg detuning ($\Delta\beta_{cb}$, cm^{-1})	-20	-32	-248.8
Injection current (I_a, mA)	53.035	53	53
Injection current (I_b, mA)	50	50	50
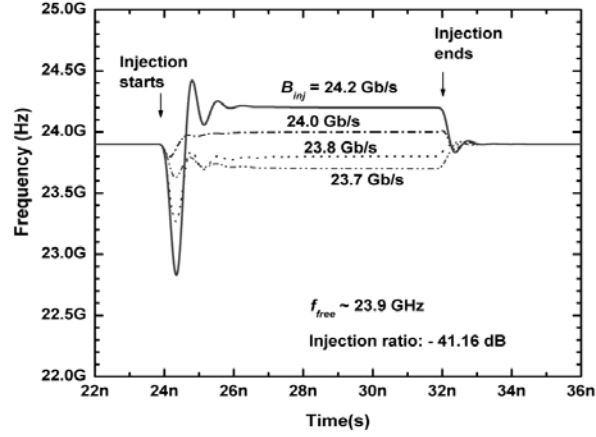
(a)
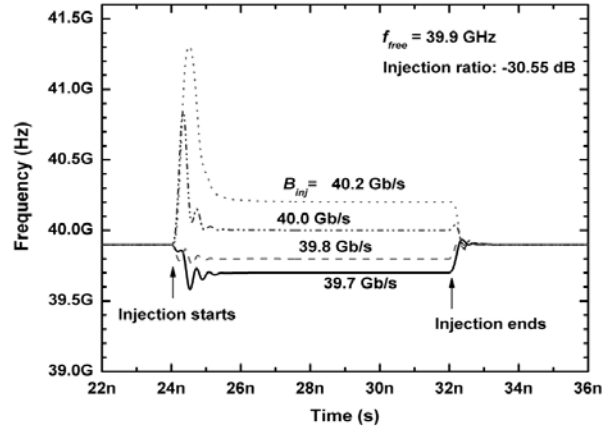
(b)
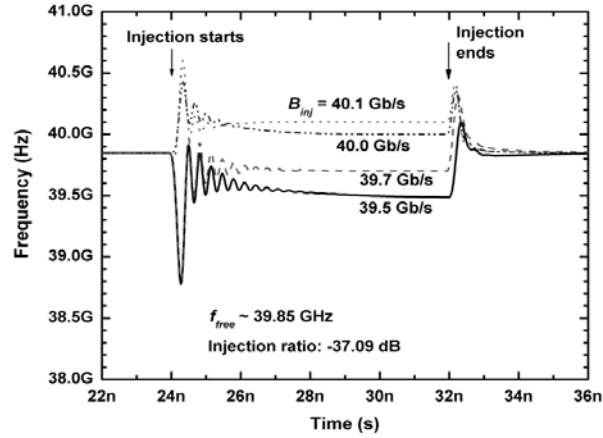
(c)

Fig. 2.4. Temporal dynamics of lockup and walk-off of coherent timing synchronization for partially gain-coupled lasers (a) and (b), and index-coupled lasers (c).

2.2.4 Lockup, walk-off and phase stability

A. Lockup and Walk-off

Simulation:

The first step in investigating the dynamics of coherent timing synchronization was to adjust the laser parameters, mainly the injection currents and the static detunings of the two sections, to achieve free-running self-pulsation at a frequency around the bit rates of interest. The optical frequencies of the two modes responsible for self-pulsation were calculated. The modal characteristics are different between the two-section index- and partially gain-coupled DFB lasers, and have been discussed in detail in [39]. The parameters for the simulation of self-pulsing TS-DFB lasers are listed on the table 2.1. The optical carrier frequency of the injected CSRZ data signal was then chosen to enable locking of the two laser modes of the TS-DFB laser responsible for self-pulsation to the clock components of the injected data signal. The injection ratio (the ratio of injected signal power to the output power of the free-running laser) was in the range of -30 dB to -46 dB. The instantaneous phase and frequency of the free-running self-pulsation and the recovered clock were calculated to analyze the dynamic behaviors of coherent timing synchronization. The calculation procedure of the instantaneous phase and frequency is given in the Appendix A [49, 50].

The simulation results for the temporal dynamics of lockup and walk-off are presented in Fig. 2.4. The injected data signal consisting of only bit 1's was turned on at 24 ns and off at 32 ns. Fig. 2.4(a) illustrates the lockup process of the self-pulsation signal in a two-section partially gain-coupled DFB laser to the injected data signals at several different bit rates around the free-running self-pulsation frequency, f_{free}, at 23.9 GHz. The injection ratio was

-41.16 dB. The lockup time was about 2 nanoseconds and the walk-off time was less than 1 nanosecond for all four cases. Now the static detunings and bias currents of the two sections were adjusted as listed on the table 2.1 so that $f_{free} = 39.9$ GHz in Fig. 2.4(b). The injection ratio was -30.55 dB. Again, about a nanosecond lockup time and sub-nanosecond walk-off time were observed. The results of the index-coupled case are in Fig. 2.4(c) for $f_{free} = 39.85$ GHz. The injection ratio was -37.09 dB. Two-section index-coupled DFB lasers also showed fast lockup and walk-off dynamics of timing synchronization. The sub-nanosecond walk-off time observed in this simulation contradicts the experimental results in [3, 22].
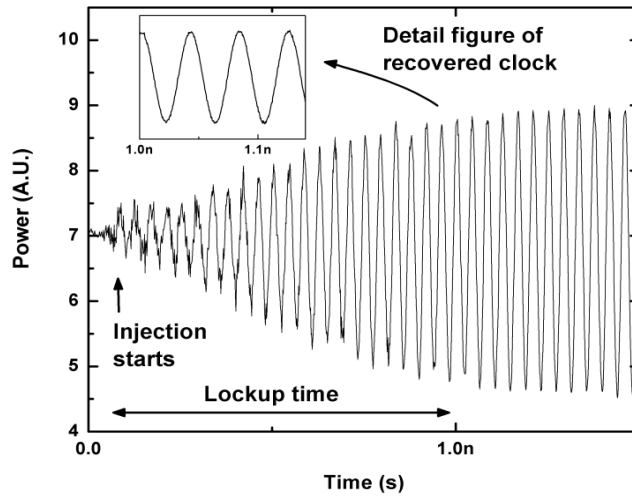
Fig. 2.5. Time-domain waveform of coherent timing synchronization in the lockup process. The inset is the averaged time-domain waveform in the steady state.

Experiment:

To investigate the lockup and walk-off time of timing synchronization experimentally, a repetitive user-defined bit pattern was injected into the TS-DFB laser. The bit rate of the input data was fixed at 24 Gb/s. The bit pattern was 2048-bit long consisting of 64 consecutive bits

24

of 1's and 1984 bits of 0's. The long series of bit 0's were chosen to ensure loss of clock synchronization before the injection of the next series of 64 bit 1's. The wavelength of the tunable laser was tuned for coherent timing synchronization. The free-running self-pulsation frequency was controlled by adjusting the injection current of the back section. The free-running self-pulsation frequency was detuned about -100 MHz from the input data rate at 24 Gb/s when the two sections were biased at $44.36\,\text{mA}$ (front section) and $20\,\text{mA}$ (back section), respectively. The output power was $0.1\,\text{mW}$ measured after the circulator. The average injection power was about $11.6\,\mu\text{W}$ before coupling into the TS-DFB laser. The coupling efficiency was estimated to be about 10%.
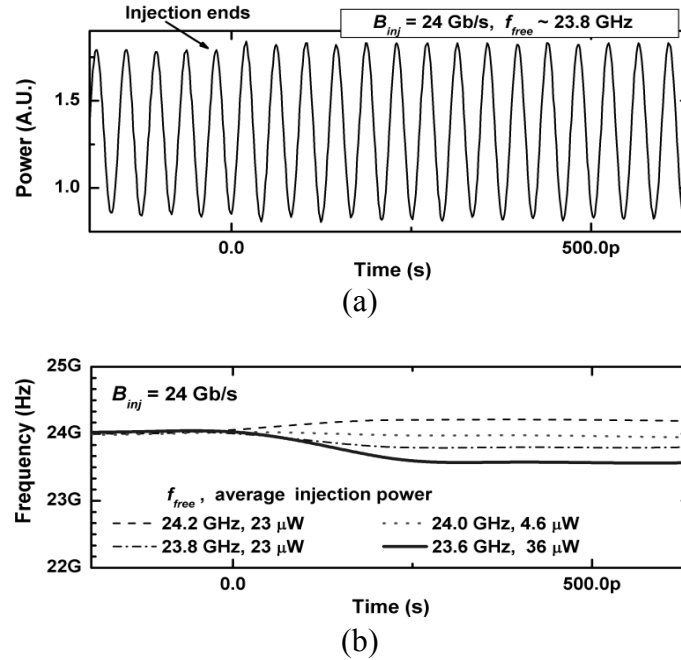
Fig. 2.6. (a) Time-domain waveform of coherent timing synchronization in the walk-off process ($B_{inj} = 24\,\text{Gb/s}$, $f_{free} \approx 23.8\,\text{GHz}$). (b) Instantaneous frequency of time-domain waveform in the walk-off process ($B_{inj} = 24\,\text{Gb/s}$).

The output signal was observed by a digital sampling oscilloscope triggered by the pattern-trigger signal from the pattern generator. When the observed signal was averaged, the amplitude of the recovered clock signal (synchronized with the trigger) was significant whereas that of the free-running self-pulsation signal was averaged out to zero. The experimental result of the lockup dynamics is shown in Fig. 2.5. After about 1 ns of injection, the amplitude of the recovered clock signal (see inset) was stabilized. Hence, the lockup time of timing synchronization was about 1 ns.

To observe the walk-off of the recovered clock at the end of the series of bit 1's, the time-domain signal was first obtained. The results are shown in Fig. 2.6(a), corresponding to $f_{free} = 23.8\,\text{GHz}$. It is easy to notice that there is a slight change of the amplitude in the time-domain signal caused by turning off the injection signal. However, it is not clear if there is any frequency or phase change in the self-pulsation signal after turning off the injection signal. In order to ascertain the frequency or phase of the self-pulsation signal, the instantaneous frequency of the measured time-domain waveform was calculated using Hilbert transformation [49, 50].

The frequency evolutions of the walk-off process of the recovered clocks for $f_{free} = 24.2\,\text{GHz}$, $24\,\text{GHz}$, $23.8\,\text{GHz}$, and $23.6\,\text{GHz}$ are shown in Fig. 2.6(b). Clearly, the recovered clock (injection-locked self-pulsation) frequency relaxes to the free-running frequency for each of the above cases with roughly the same sub-nanosecond time constant.

26
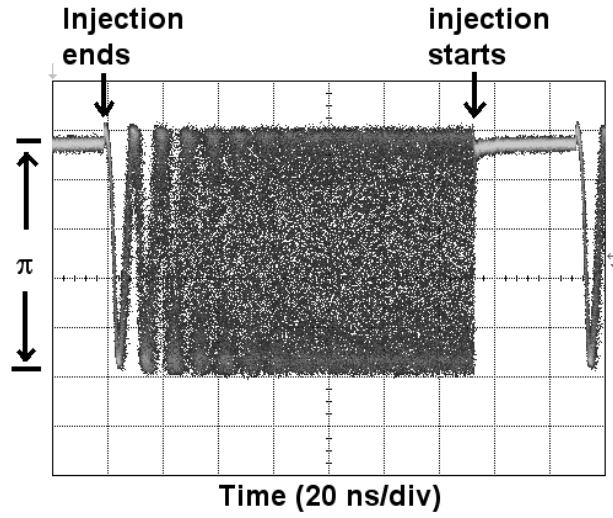
(a)
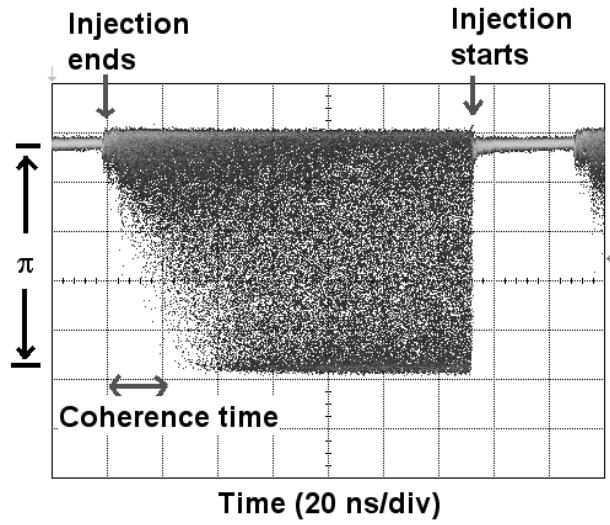
(b)

Fig. 2.7. Low-pass-filtered output signal from the harmonic mixer corresponding the phase error between the recovered clock and the data clock ($B_{inj} = 24\,\text{Gb/s}$). (a) $f_{free} \approx 23.9\,\text{GHz}$, $\Delta f \approx 100\,\text{Mb/s}$. (b) $f_{free} \approx 24\,\text{GHz}$, $\Delta f \approx 0$.

To confirm the dynamics of walk-off, the recovered clock signal was mixed with the clock signal from the pattern generator in a harmonic mixer. The low-pass-filtered output signal, which corresponds to the phase difference between the recovered clock and the clock of the pattern generator, was observed on the sampling oscilloscope in the eye-mode. The bit pattern was 4098-bit long consisting of 896 consecutive bits of 1's and 3202 consecutive bits of 0's.

Fig. 2.7(a) shows the observed signal when $f_{free} = 23.9 \, \text{GHz}$. The average injection power was $65 \, \mu\text{W}$ before coupling into the TS-DFB laser. The output signal started to oscillate at $100 \, \text{MHz}$, which is exactly the detuning frequency $(\Delta f = B_{inj} - f_{free})$. This shows clearly that the TS-DFB laser relaxes to free-running state instantly when the injection signal is turned off. It is also observed that the oscillations smeared out gradually and became invisible after about $20 \, \text{ns}$. The smearing is due to the fact that the free-running self-pulsation frequency drifts randomly due to spontaneous emission noise, which is not included in our simulation model.

Fig. 2.7(b) shows the phase error when the bit rate of the input data was the same as the free-running self-pulsation frequency. Broadening of the phase error after turning off the injection signal was observed. However, there were no oscillations since the bit-rate detuning was zero. Fig. 2.7(b) shows the coherence time of the free-running self-pulsation signal is on the order of $20 \, \text{ns}$ when the self-pulsation signal becomes out of phase with respect to the recovered clock signal.
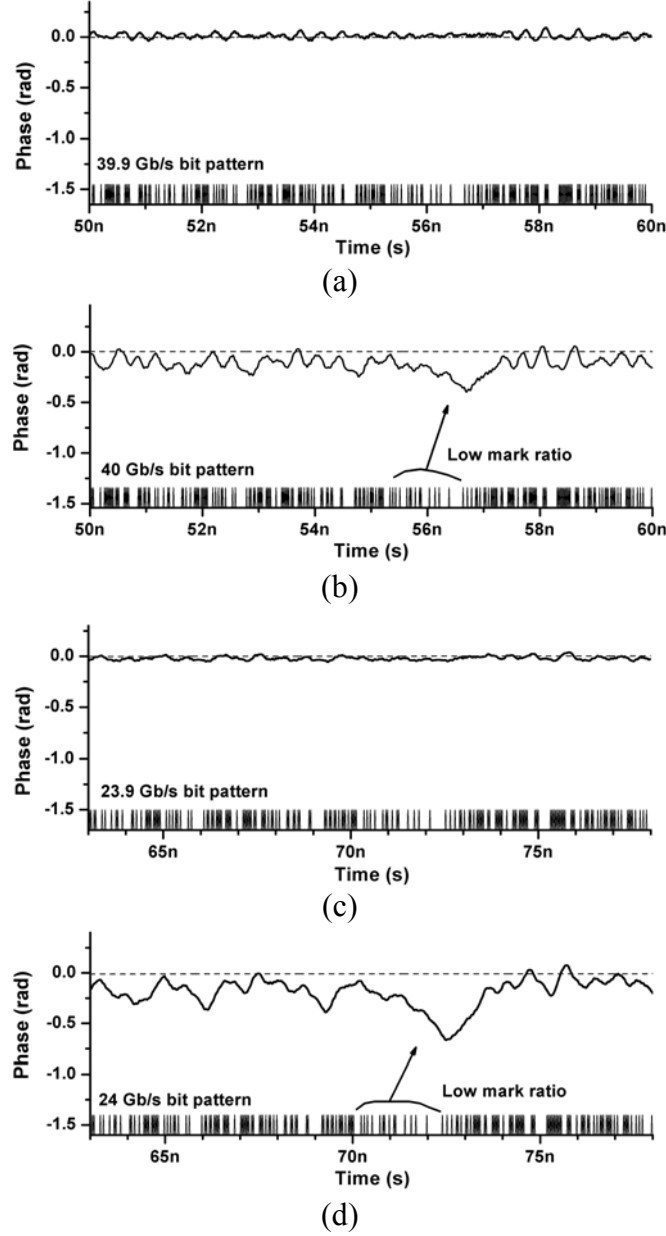
Fig. 2.8. Phase of the recovered clock with the injection of PRBS data (solid lines). The locked phase under the injection of consecutive bits of 1's is set to zero (dashed lines). (a) $f_{free} = 39.9\,\text{GHz}$, $B_{inj} = 39.9\,\text{Gb/s}$. (b) $f_{free} = 39.9\,\text{GHz}$, $B_{inj} = 40\,\text{Gb/s}$. (c) $f_{free} = 23.9\,\text{GHz}$, $B_{inj} = 23.9\,\text{Gb/s}$. (d) $f_{free} = 23.9\,\text{GHz}$, $B_{inj} = 24\,\text{Gb/s}$.

B. Phase Stability with PRBS Signal Injection

Simulation:

To investigate the phase stability of the recovered clock, PRBS data was injected into the TS-DFB laser in simulation. Fig. 2.8 shows the simulation results of the phase stability of the recovered clock when a $2^{10}-1$ PRBS signal was injected into the TS-DFB laser. This length of PRBS data was chosen so that computation time was reasonable. Fig. 2.8(a) and (b) were for timing synchronization operation around $40\,\text{Gb/s}$ with $f_{free} = 39.9\,\text{GHz}$. Fig. 2.8(c) and (d) were for timing synchronization operation around $24\,\text{Gb/s}$ with $f_{free} = 23.9\,\text{GHz}$. A comparison of the four cases in Fig. 2.8 at different bit rates and bit-rate detunings leads to the following observations, which are consistent with the results in the previous section. First, the magnitude of the phase fluctuation increases when the mark ratio of the input data is low for the case of nonzero bit-rate detuning. Second, the phase of the recovered clock is more stable when the bit-rate detuning is smaller. Third, for the same bit-rate detuning, the phase of the recovered clock is more stable when the bit rate is higher.

Experiment:

In the experiments, $2^{15}-1$ pseudo-random 2-bit word pattern at 24 Gb/s was injected into a TS-DFB laser. Phase fluctuation of the recovered clock was measured as described in the previous section. The average injection power was about 89 μW before coupling to the TS-DFB laser. Fig. 2.9(a) and (b) show the experimentally measured phase fluctuation of the recovered clock for the cases of bit-rate detuning of zero and $100\,\text{Mb/s}$, respectively. The experimental results agree well with the simulation results.
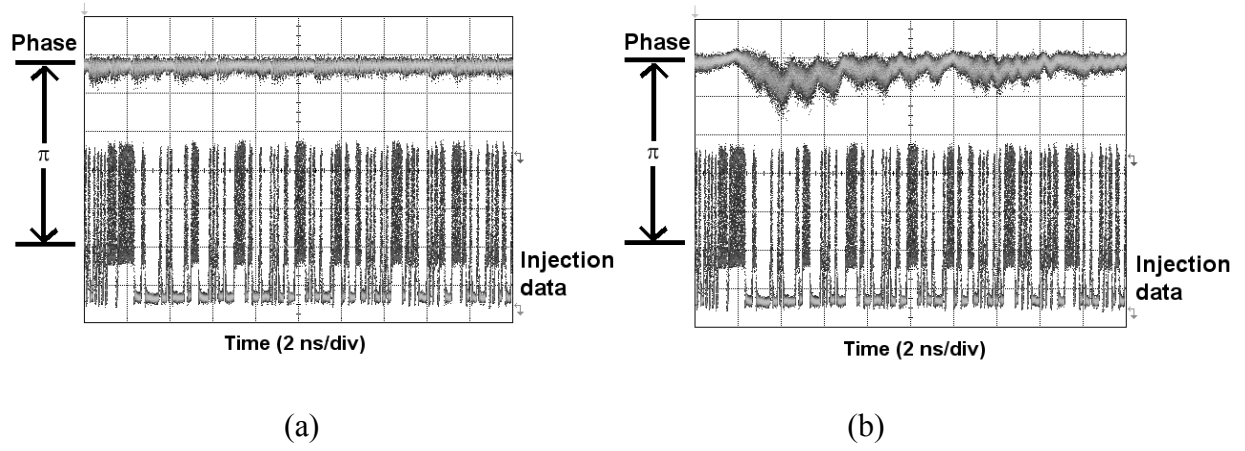
Fig. 2.9. Low-pass-filtered output signal from the harmonic mixer (corresponding the phase error between the recovered clock and the data clock) and the bit pattern of the PRBS data ($B_{inj} = 24\,\text{Gb/s}$). (a) $f_{free} \approx 24\,\text{GHz}$, $\Delta f \approx 0$. (b) $f_{free} \approx 23.9\,\text{GHz}$, $\Delta f \approx 100\,\text{Mb/s}$.

Summary:

Both simulation and experimental results showed nanosecond lockup time for the coherent timing synchronization. This ultrafast lockup is a desirable property that will reduce system latency. The lockup time could be reduced to less than 1 ns by increasing injection power [48]. However, the relaxation oscillation amplitude in the lockup process increases as the injection power increases, as a result the recovered clock signal will be more pattern dependent. The injection power level should be optimized to balance lockup time and pattern dependence. Walk-off time, on the other hand, doesn't depend on the injection signal but rather the dynamic behavior of the free-running TS-DFB laser only.

Even though the walk-off time is only on the order of 1 ns , the coherent timing synchronization scheme can operate for input data patterns consisting of spaces (consecutive bits of 0's) much longer than 1 ns in duration. When the bit-rate detuning is zero, the dephasing time

31

is dominated by the coherence time of the free-running self-pulsation signal which is on the order of $20\,\mathrm{ns}$. When the bit-rate detuning is large, the dephasing time is inversely proportional to the bit-rate detuning. This result was quite similar to the case of timing synchronization using a self-pulsation laser diode [51]. The dephasing speed is about $2\pi\Delta f\,\mathrm{rad/sec}$. So the maximum phase change will be about $2\pi\Delta f N_{0's}/B_{inj}$ where $N_{0's}$ is the length of the longest series of bit 0's in data and Δf is the bit-rate detuning. If we assume nominally that 5 % clock phase error is acceptable, the bit-rate detuning, $|\Delta f|$, should be in the range of $0.05 B_{inj}/N_{0's}$.

2.2.5 Phase stability tolerance

Based on the substantial agreement of the deterministic timing synchronization behaviors between simulations and experiments presented in the previous section, we now proceed to predict the dynamic behaviors of all-optical coherent timing synchronization using TS-DFB lasers that are important for applications in optical packet switching such as all-optical packet regeneration and burst-mode receivers. In both cases, the incoming packets may have different phases, wavelengths, average powers, and slightly different bit rates. The recovered clock must maintain its phase relationship with respect to the incoming packet for the above variations.

With all other conditions fixed, the recovered clock maintains its phase relationship with the phase of the input data since coherent timing synchronization using TS-DFB lasers is an open-loop operation [52]. However, this phase relationship (between the recovered clock and the input data) is expected to be dependent on the power as well as the wavelength of the injection signal. This can be understood from injection locking between a master laser and a slave laser [45-48]. The optical phase difference between the injection-locked slave laser and master laser

depends on the injection ratio and the wavelength detuning. As a result, the phase of the recovered clock, which is determined by the phase of each of the injection-locked modes of the TS-DFB laser, will depend on the injection power, which changes the injection ratio, and the data wavelength which changes the detuning.
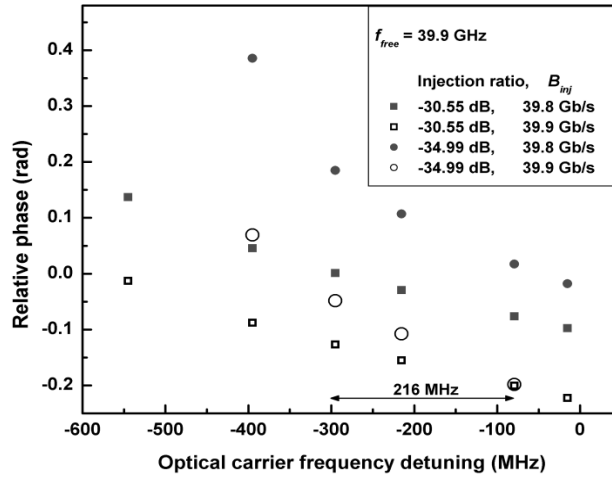
Fig. 2.10. Phase of the recovered clock relative to the phase of the input data as a function of the optical carrier frequency detuning (i.e., wavelength detuning).

To investigate the robustness of coherent timing synchronization due to wavelength drift of the injected signal, the optical carrier frequency of the injected data signal was varied while fixing the data rate.

In Fig. 2.10, the phase of the recovered clock is plotted against the optical carrier frequency detuning of the injected data signal. The optical carrier frequency detuning is obtained by subtracting the center frequency of the free-running self-pulsation signal from the optical carrier frequency of the injection signal. The injected data rates were fixed at 39.8 Gb/s or 39.9 Gb/s with f_{free} = 39.9 GHz so that the bit-rate detuning was -100 Mb/s or zero respectively. The

33

simulation parameters of the two-section partially gain-coupled DFB laser are listed on the table 2.1. The injection ratio was $-30.55\,\text{dB}$ or $-34.99\,\text{dB}$. At these low injection levels, successful clock recovery requires negative wavelength detuning. This is consistent with the asymmetric behavior in optical injection locking [3]. The phase of the recovered clock changed by about $0.17\,\text{radian}$ ($0.08\,\text{radian}$) when the optical carrier frequency was varied by $216\,\text{MHz}$ at an injection ratio of $-34.99\,\text{dB}$ ($-30.55\,\text{dB}$) with $-100\,\text{Mb/s}$ bit-rate detuning. With zero bit-rate detuning, the phase of the recovered clock changed by $0.15\,\text{radian}$ ($0.07\,\text{radian}$) when the optical carrier frequency was varied by $216\,\text{MHz}$ at an injection ratio of $-34.99\,\text{dB}$ ($-30.55\,\text{dB}$). Smaller phase change of the recovered clock at higher injection ratio is consistent with the theory and operation of optical injection locking [3]. If we assume nominally that 5 % clock phase error is acceptable, a 730 MHz drift of optical carrier frequency (wavelength drift of $0.0058\,\text{nm}$ at $1550\,\text{nm}$) is acceptable in the case of zero bit-rate detuning at the injection ratio of $-30.55\,\text{dB}$.
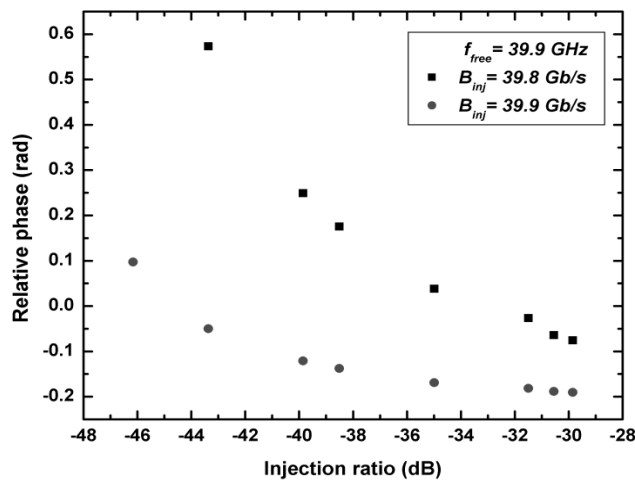
Fig. 2.11. Phase of the recovered clock relative to the phase of the input data as a function of the injection ratio.

34

Fig. 2.11 shows the phase of the recovered clock relative to the phase of the input data as a function of the injection ratio. The input data rates was 39.8 Gb/s or 39.9 Gb/s with $f_{free} = 39.9\,\text{GHz}$. The optical carrier frequency of the injection signal was at $-115.2\,\text{MHz}$ from the center frequency of the free-running self-pulsation signal. For a 10 dB change from - 40 dB to -30 dB in injection ratio, the phase of the recovered clock varied by 0.33 radian (0.07 radian) with a bit-rate detuning of $-100\,\text{Mb/s}$ (zero). The dynamic range is about 17 dB for a 5 % clock phase error when the bit-rate detuning is zero.

In packet switched networks, optical packets may also vary in bit rate from a nominal rate. With all other conditions unchanged, the injected data signal with slightly different bit rates were injected into the laser. Fig. 2.12 plots the relative phase between the recovered clock and the input data as a function of the injected bit rate. The optical carrier frequency of injected data signal was again fixed at -115.2 MHz from the center frequency of the free-running self-pulsation signal. A relative phase change of 0.21 radian (0.12 radian) was observed for a bit variation of 100 Mb/s at the injection ratio of -34.99 dB (-30.55 dB). The acceptable bit-rate variation is 260 Mb/s for a 5 % clock phase error when the injection ratio is -30.55 dB.

35
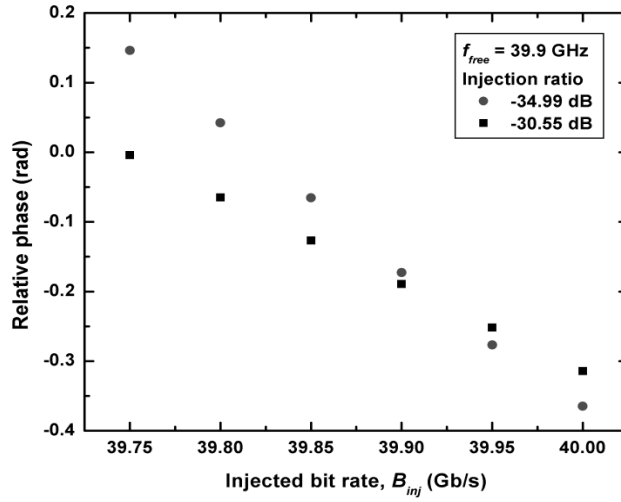
Fig. 2.12. Phase of the recovered clock relative to the phase of the input data as a function of the bit rate of injected data.

2.2.6. Summary

The dynamics of all-optical coherent timing synchronization using TS-DFB lasers have been studied by numerical simulation and experiment. Both simulation and experimental results showed lockup time and walk-off time about 1 nanosecond. The walk-off dynamics of timing synchronization depends on the dynamic property of the TS-DFB laser but the lockup dynamics is slightly modified depending on the injected signal power and wavelength detuning. Fast lockup of coherent timing synchronization is preferable since it will reduce the system latency. Sub-nanosecond walk-off, on the other hand, can be problematic for input data patterns that contain long series of bit 0's. The dephasing speed for the injection signal of the consecutive bits of 0's in data was proportional to the bit-rate detuning. The bit-rate detuning should be smaller than $0.05 B_{inj} / N_{0's}$ to ensure less than 5 % timing error. As the clock frequency increases the allowed bit-rate detuning also increases when the length of the longest series of bit 0's is fixed.

Since coherent timing synchronization using TS-DFB lasers is an open-loop operation, the recovered clock maintains its phase relationship with the phase of the input data. Coherent timing synchronization using TS-DFB lasers is found to be suitable for applications in ultrafast-optical packet switching. When the bias conditions of the TS-DFB laser are optimized for a specific bit rate with consecutive bits of 1's, 5 % phase stability of the recovered clock can be maintained for an input power dynamic range of $17\,\mathrm{dB}$, or bit-rate fluctuation of $260\,\mathrm{Mb/s}$, or optical carrier frequency drift of $730\,\mathrm{MHz}$ (wavelength drift of $0.0058\,\mathrm{nm}$).

2.3 180 GHz all-optical timing synchronization

2.3.1 Introduction

Ultrafast clock recovery (timing synchronization) is an essential element for future optical communications. To achieve optical retiming, reshaping, and re-amplification (3R regeneration), timing synchronization at the aggregate line rate is required. Some experiments have been performed to extract a sub-harmonic clock from a 160-Gb/s data which is useful for optical time-division demultiplexing [53, 54]. Recently, all-optical timing synchronization at the line rate from 160-Gb/s data was demonstrated using mode-locked laser diodes [24, 55]. It required high injection power above 1 dBm to induce adequate gain modulation in the mode-locked laser, which caused pattern effect. The additional post filter was used to remove the residual pattern from the recovered clock. The additional drawback of the mode-locked laser is that the mode-locking frequency is restricted by the device length. The self-pulsing multi-section gain-coupled (MS-GC) DFB laser is used for all-optical timing synchronization because of its compactness

and wide tuning range. In addition, coherent timing synchronization has negligible pattern effect because it works with low injection power.
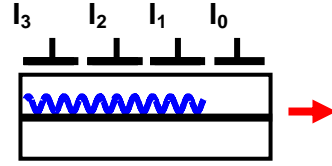
(a)
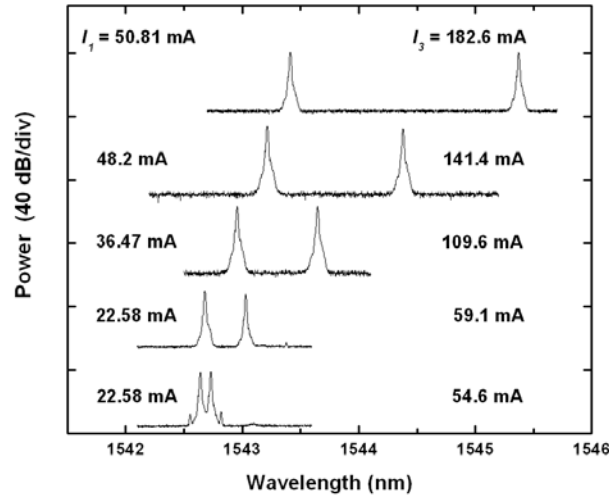
(b)

Fig. 2.13. (a) Device structure of the MS-GC DFB laser, (b) Optical spectra of the self-pulsation signals for different injection currents of the first section (I_1) and the third section (I_3); $I_2 = 21$ mA.

2.3.2 Wide tunable multi-section gain-coupled DFB lasers

The device structure is shown on the Fig. 2.13(a). The width of the waveguide was 2 μm. Each section was about 395-μm-long and separated by 6 μm for electrical isolation. The output facet of the SOA section was anti-reflection coated. The MS-GC DFB laser was temperature controlled and was set to 21.5 ^{o}C. Self-pulsations result from beating of the lasing modes in the first and third sections, respectively. Tuning of the self-pulsation frequency can be accomplished by adjusting the injection currents I_1 and I_3, Fig. 2.13(b).

The red shift of the spectral peaks was due to increased indices of the DFB gratings as a result of thermal effects when the injection currents were increased [56]. Because of the separation of the first and third sections by the transparent middle section, the two lasing modes responsible for self-pulsation are much better thermally isolated as compared to a TS-DFB laser which has two DFB sections adjacent to each other. As a result, the red shift of the lasing mode of the first section will be smaller when the injection current into the third section was increased compared to the TS-DFB laser.

The minimum frequency of the self-pulsation was about 12 GHz and the maximum frequency was about 246 GHz. In comparison, the highest self-pulsation frequency in a two-section GC DFB laser was 120 GHz [30]. Self-pulsation at 180 GHz was obtained by setting $I_0 =$ 46.55 mA (for the SOA section), $I_1 = 50.81$ mA, and $I_3 = 162$ mA. The fiber-coupled optical power was -9.5 dBm.

2.3.3 Experimental setup and results

The schematic of the experimental setup is shown in Fig. 2.14. A 180-GHz return-to-zero (RZ) clock pulse train was generated using an electro-absorption modulator and optical filters. The electro-absorption modulator generated harmonic sidebands of the driving signal at 45 GHz. The 2nd order sidebands of the modulated optical signal on each side were selected by using an optical comb filter and a tunable bandpass filter. The 180-GHz RZ pulse train had optical clock components at 1543.322 nm and 1544.754 nm, when the wavelength of tunable laser at the transmitter was set to 1544.038 nm. This RZ pulse train was modulated with a 45-Gb/s NRZ (non-return-to-zero) data stream from the pulse pattern generator. As a result, a 2^{15}-1 pseudo-random 4-bit words sequence at 180-Gb/s RZ data was generated.

The extinction ratio of the modulator (MOD in Fig. 2.14) was about 11 dB. The 180-Gb/s RZ data was injected into the MS-GC DFB laser via a circulator. A polarization controller was used before the injection of the data into the MS-GC DFB laser, since the coherent timing synchronization is polarization sensitive [3, 23]. However, it can be rendered polarization and wavelength insensitive if ultrafast polarization-insensitive wavelength conversion is performed before injection into the MS-GC DFB laser [40]. Wavelength conversion will also improve the optical clock components of the injection signal by removing the phase uncertainties of the individual OTDM (optical time-division multiplexer) channels [23].
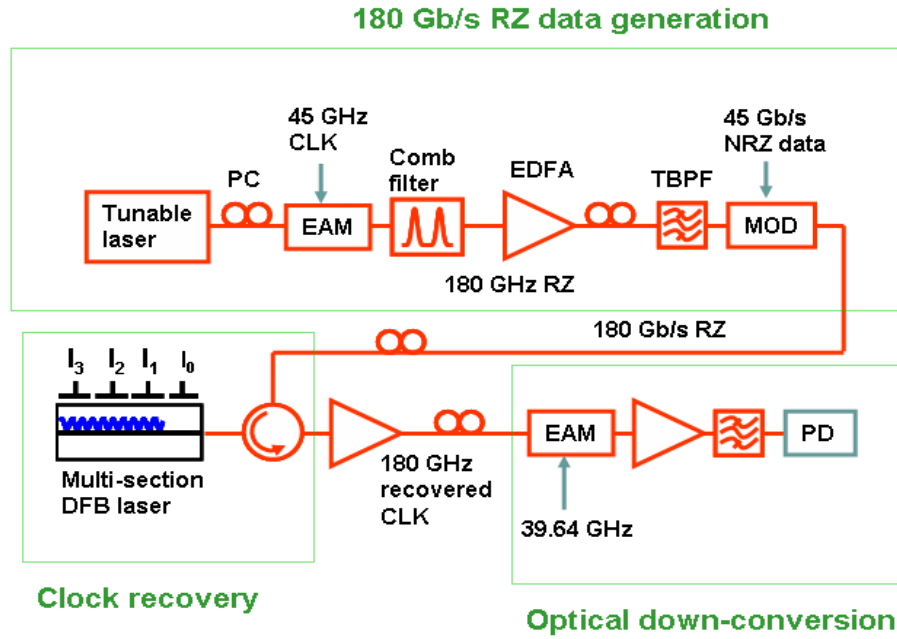
Fig. 2.14. Experimental setup for 180-Gb/s all-optical timing synchronization. PC: polarization controller. EAM: Electroabsorption modulator, MOD: LiNbO$_3$ modulator, TBPF: Tunable bandpass filter, PD: Photodetector.

The free-running self-pulsation and the recovered optical clock signal from the MS-GC DFB laser were observed in the radio-frequency (RF) spectral domain by an optical down-conversion technique, where an electro-absorption modulator was driven by a 39.64-GHz signal. As a result, the free-running self-pulsation and the recovered clock signal were down converted by 158.56 GHz (= 4 x 39.64 GHz). The down-converted signal was then detected by a 60-GHz photodetector and an RF spectrum analyzer.
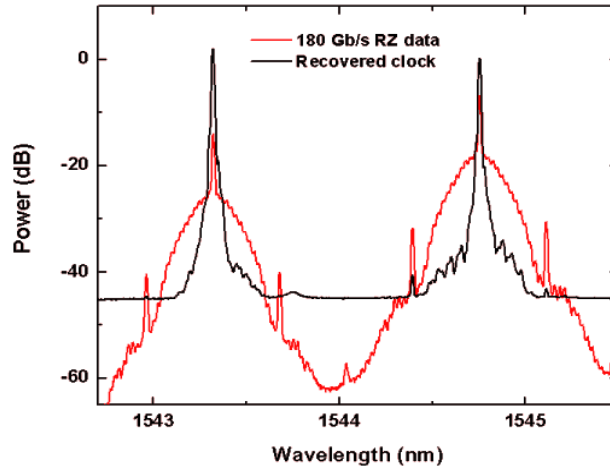
Fig. 2.15. Optical spectra of the injection data after equalization and the recovered clock from the MS-GC DFB laser with 0.1-nm resolution.

Fig. 2.15 presents the optical spectra of the injection data and the recovered clock. Two optical clock components at 1543.322 nm and 1544.754 nm were observed in the optical spectrum of the injection data. The pedestals around these optical clock components were due to data modulation at 45 Gb/s. The power in the two optical clock components were adjusted using a tunable bandpass filter to equalize the injection ratios into each lasing section since the coupling efficiency of the first section and the third section were different. Equalization of injection ratios in the two sections lead high-quality recovered clock [3]. The optical spectrum of the recovered clock reveals suppressed pedestal caused by data modulation as compared to the optical spectrum of the injection data.
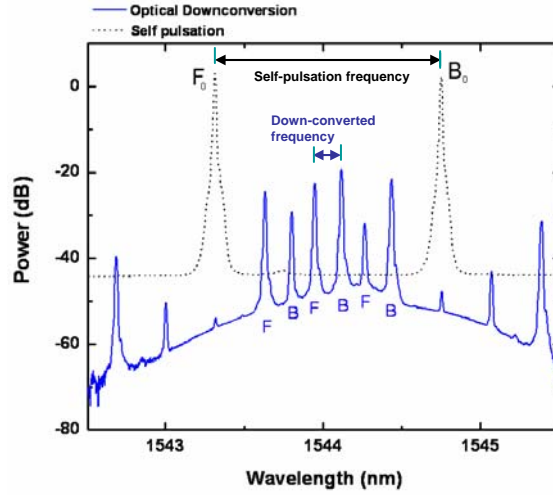
Fig. 2.16. Optical spectra of self-pulsation signal and down-converted signal.

Fig. 2.16 shows the optical spectra of the self-pulsation signal and the down-converted signal. The lasing spectral peaks of the first and third section were suppressed by optical filtering after optical down-conversion, which improves the signal to noise ratio of the RF signal because of reduced shot noise. The blue-line optical modes labeled 'F' are sidebands of the spectral peak labeled 'F_0' from the first section. The blue-line optical modes labeled 'B' are sidebands of the spectral peak labeled 'B_0' from the third section.

Fig. 2.17(a) shows the RF spectra of the self-pulsation signal and the recovered clock signal after optical down-conversion by 158.56 GHz using the electro-absorption modulator. The optical power of the injection data measured before the circulator was -1 dBm for the RF spectrum of the recovered clock in Fig. 2.17(b). The spectral peak of the free-running self-pulsation was not well defined and it had a broad linewidth. A narrow linewidth recovered clock signal, down-converted to 21.44 GHz (= 180 GHz – 158.56 GHz), with a carrier-to-noise ratio of about 40 dB was obtained at 1-MHz resolution bandwidth.
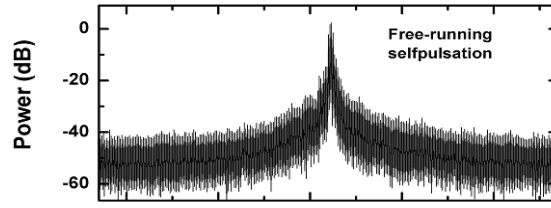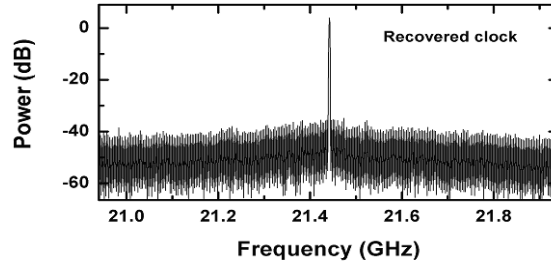
Fig. 2.17. (a) RF spectra of the down-converted free-running self-pulsation, (b) optically recovered clock; resolution bandwidth = 1 MHz.

In order to assess the quality of the recovered clock compared to the 180-GHz optical clock (RZ pulse train without data modulation), the phase noise of the down-converted signal was measured to quantify the jitter of the recovered clock. Fig. 2.18(a) presents the phase noise spectra of the down-converted recovered clock signal and the 180-GHz RZ pulse train without data modulation. The optical power of the injection data was -1 dBm. The root-mean-square (rms) timing jitter was calculated by integrating the phase noise from 100 Hz to 10 MHz. The rms timing jitter of the 180-GHz RZ pulse train without data modulation was 356 fs and that of the recovered clock was 403 fs at the injection power of -1 dBm. The dynamic range of this timing synchronization scheme was from -8 dBm to -1 dBm, Fig. 2.18(b). Within this dynamic range, the recovered clock maintains a timing jitter of less than 410 fs.

44
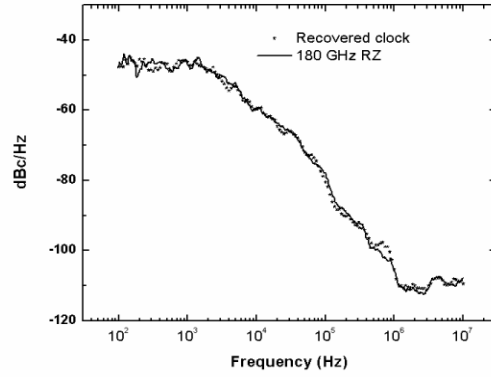
(a)
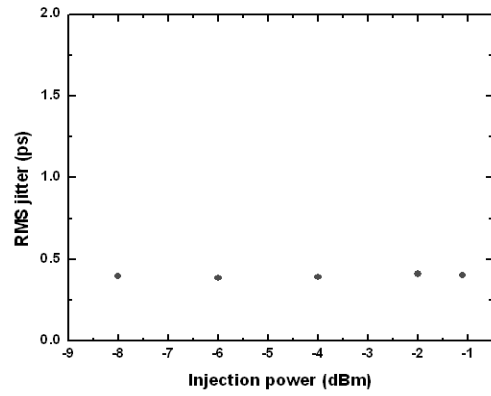
(b)

Fig. 2.18. (a) Phase noise of the 180-GHz RZ pulse train and recovered clock measured at the down-converted frequency (21.44 GHz), (b) RMS jitter vs. injection power.

2.3.4 Summary

The MS-GC DFB laser exhibits self-pulsation over a tuning range of more than 230 GHz, which enables all-optical timing synchronization at high bit rates. All-optical timing synchronization at

180 GHz has been demonstrated utilizing this MS-GC DFB laser. The recovered clock has a jitter of less than 410 fs over a dynamic range of 7 dB.

CHAPTER 3: PHASE AND POLARIZATION SYNCHRONIZATION

3.1 Introduction

Coherent optical communication has attracted renewed interest in recent years. Carrier phase recovery remains one of the challenges for coherent detection, in part, due to the fact coherent modulation format including phase-shift keying (PSK) is carrier-suppressed in nature. Without the presence of the optical carrier the most straightforward phase recovery techniques, including injection locking and phase-locked loops (PLL), cannot be applied directly. There have been demonstrations of carrier phase recovery using decision-driven (DD) PLL [32]. The high bandwidth required of DD-PLL is difficult to achieve for practical purposes. Recently, digital feed-forward techniques have been proposed for carrier-phase estimation [11, 34]. Both DD-PLL and digital carrier phase recovery, however, still require polarization alignment/diversity. In addition, novel all-optical signal processing techniques for coherent modulation formats such as regeneration of PSK require a polarization and phase locked local oscillator [9, 10].

In this section, we present, for the first time, simultaneous recovery of both carrier phase and polarization from a carrier-suppressed PSK signal all-optically. This is achieved by using a PSK data-pumped phase-sensitive oscillator (PSO). The PSO is a degenerate optical parametric oscillator that has a phase sensitive amplifier (PSA) as a gain block. The PSA can be configured as a nonlinear Mach-Zehnder interferometer (NMZI) or nonlinear optical loop mirror (NOLM).

Section 3.2.1 explains the operation principle of the phase sensitive amplifier in the form by a NMZI (or NOLM). Section 3.2.2 present the small signal gain of phase sensitive amplification and phase insensitive amplification in the NMZI (or NOLM). Section 3.2.3 analyzed the stability

tolerance of the PSO. Section 3.2.4 presents the experimental results of all-optical carrier synchronization. Section 3.2.5 is the summary of the work.

3.2 All-optical carrier synchronization using a phase sensitive oscillator

3.2.1 Phase sensitive amplifier
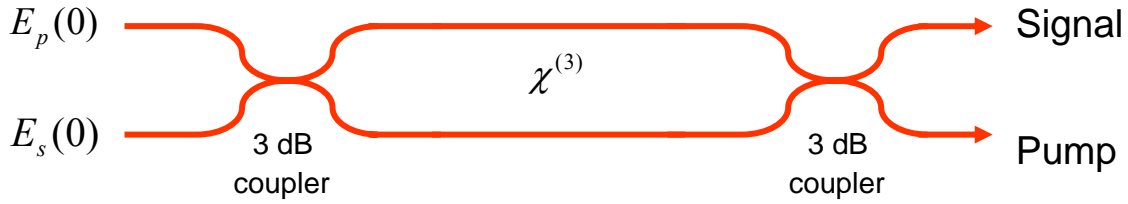
Fig. 3.1. Configuration of NMZI

Fig. 3.1 shows the schematic diagram of PSA made by NMZI [57]. The pump, E_p, and signal, E_s, have the same wavelength and are phase locked. When both of the pump and signal are present, different amounts of nonlinear phase shifts are accumulated in the two paths because the pump and signal interfere constructively (destructively) in one (the other) path. The difference in nonlinear phase shifts between the two paths $\phi_{NL} = \gamma L |E_p(0)||E_s(0)| \sin(\phi_{p0} - \phi_{s0})$, which is phase sensitive, breaks the balance between the two paths leading to the coupling between the pump and signal.

The output signal at the signal port is given by

$$E_s(L) = ie^{i\phi_0}(|E_s(0)|e^{i\phi_{s0}}\cos\phi_{NL} + |E_p(0)|e^{i\phi_{p0}}\sin\phi_{NL}),\tag{3.1}$$

where $\phi_0 = \gamma L(|E_p(0)|^2 + |E_s(0)|^2)/2$ is the phase insensitive nonlinear phase shift [57]; L is the amplifier length (= the length of interferometer); ϕ_{p0} and ϕ_{s0} are the input pump and signal phases respectively; γ is the fiber nonlinear coefficient.

The output signal power is given by

$$P_s = P_{s0}\cos^2\phi_{nl} + P_{p0}\sin^2\phi_{nl} + \sqrt{P_{s0}P_{p0}}\sin(2\phi_{nl})\cos(\phi_{p0} - \phi_{s0}),\tag{3.2}$$

where $P_{p0} = |E_p(0)|^2$ and $P_{s0} = |E_p(0)|^2$ are the input signal and pump powers respectively. The gain of PSA is phase sensitive. When the initial phase difference between pump and signal is $\pi/2$ or $3\pi/2$, the phase-sensitive nonlinear phase shift is maximized. However, when the difference is 0 or π, there is no phase-sensitive nonlinear phase shift. From Eq (3.1), it is observed that the PSA gain has a two-fold symmetry with respect to the pumping phase. Specifically, the output signal $E_s(L)$ has the same output phase and amplitude for the pumping phases of ϕ_{p0} and $\phi_{p0} + \pi$. Therefore a CW signal can be amplified by the PSA with either a CW pump or, interestingly, a BPSK pump.

3.2.2 Small signal gain

It is important to point out that the NMZI (or NOLM) can also provide phase-insensitive (non-degenerate FWM (NDFWM)) gain. So, it is necessary to identify the small signal gain of the NMZI (or NOLM) for DFWM and NDFWM processes which provide phase sensitive amplification and phase insensitive amplification, respectively.

The coupled equations of electric field in the NMZI for un-depleted pump can be written as

$$\frac{dE_{p,n}(z)}{dz} = i\gamma P_{p,n} E_{p,n}(z)$$

$$\frac{dE_{s,n}(z)}{dz} = 2i\gamma P_{p,n} E_{s,n}(z) + i\gamma E_{a,n}^{*}(z) E_{p,n}^{2}(z) e^{-i\Delta k z} \qquad (3.3)$$

$$\frac{dE_{a,n}(z)}{dz} = 2i\gamma P_{p,n} E_{a,n}(z) + i\gamma E_{s,n}^{*}(z) E_{p,n}^{2}(z) e^{-i\Delta k z},$$

where subscript $n = 1$ (or 2) indicates the upper (or lower) branch of the NMZI. $E_a(Z)$ is the field of idler. The energy conservation requires $\Delta\omega = \omega_p - \omega_s = \omega_p - \omega_a$ where ω_p, ω_s, ω_a and are the angular frequencies of the pumping, signal, and idler, respectively. It is assumed that the optical frequency of the signal and idler are very close to the pump that $\Delta kL = \beta_2 \Delta\omega^2 L \ll 1$ where β_2 is group velocity dispersion. The initial conditions are given by $E_{a,n}(0) = 0$, $E_{s,n}(0) = i^{2-n} E_s(0)/\sqrt{2}$, $E_{p,n}(0) = i^{n-1} E_p(0)/\sqrt{2}$, and $P_{p,n} = |E_{p,n}(0)|^2$ at $z = 0$; just after the first 3 dB coupler in Fig. 3.1.

The fields after propagation of $z = L$ are given by

$$E_{p,n} = E_{p,n}(0)e^{i\gamma P_{p,n}L}$$
$$E_{s,n} = (1+i\gamma P_{p,n}L)E_{s,n}(0)e^{i\gamma P_{p,n}L} \qquad (3.4)$$
$$E_{a,n} = i\gamma P_{p,n}L \, E_{s,n}(0)e^{-2i(\phi_{s0}-\phi_{p0})}e^{i\gamma P_{p,n}L}.$$

The electric fields at the signal output port just after the 3 dB coupler ($z = L$) are given by

$$E_s(t) = \sqrt{P_s}\, i e^{i(\phi_{p0}+\gamma P_p L/2)}\left(1+\frac{1}{2}i\gamma P_{p0}L\right)e^{i(\phi_s-\phi_p)}e^{i\omega_s t}$$
$$E_a(t) = \sqrt{P_s}\, e^{i(\phi_{p0}+\gamma P_p L/2)}\left(\frac{1}{2}\gamma P_{p0}L\right)e^{-i(\phi_s-\phi_p)}e^{i\omega_a t}. \qquad (3.5)$$

The total field can be rewritten as

$$E_s(t)+E_a(t) = ie^{i\gamma P_p L/2}(E_s(0)e^{-i\Delta\omega t} + E_p(0)\gamma L|E_p(0)||E_s(0)|\sin(\phi_{p0}-\phi_{s0}+\Delta\omega t))e^{i\omega_p t}. \quad (3.6)$$

If we assume $P_{s0} \ll P_{p0}$, $\gamma L|E_p(0)||E_s(0)| \ll 1$ for un-depleted pumping and assume $\Delta\omega = 0$ for DFWM, the result agrees with Eq. (3.1). These results can be used for estimation of the small signal gain of the NMZI.

The small signal gain of the signal E_s for phase insensitive amplification is

$$1+G^2, \quad where \; G = \frac{1}{2}\gamma P_p L \qquad . \qquad (3.7)$$

The small signal gain of the phase sensitive amplification can be found from the above Eq. (3.6) by making the signal and idler have the same optical frequency. The maximum small gain is

$$1+2G^2+2G\sqrt{1+G^2} \quad (\max). \tag{3.8}$$

Therefore, when the NMZI/NOLM is placed in the cavity to form an oscillator, the phase sensitive process will be dominant as it has a lower pump threshold. At the same time, the polarization of the oscillating signal will be aligned to the pump since FWM is polarization sensitive, too. In summary, an optical carrier with the same polarization and phase as the pump will oscillate in a phase-sensitive oscillator when it is pumped by a BPSK signal.

A VPI photonics simulator was used to verify the theory. The pumping power was 20 mW, the input signal power was 0.5 mW and $\gamma L\, P_{p0} = 3.24$. The optical frequency difference between the signal and the pump was 2 GHz for phase insensitive amplification. Fig. 3.2 shows the optical spectra at the signal port depend on the amplification processes and the pumps.
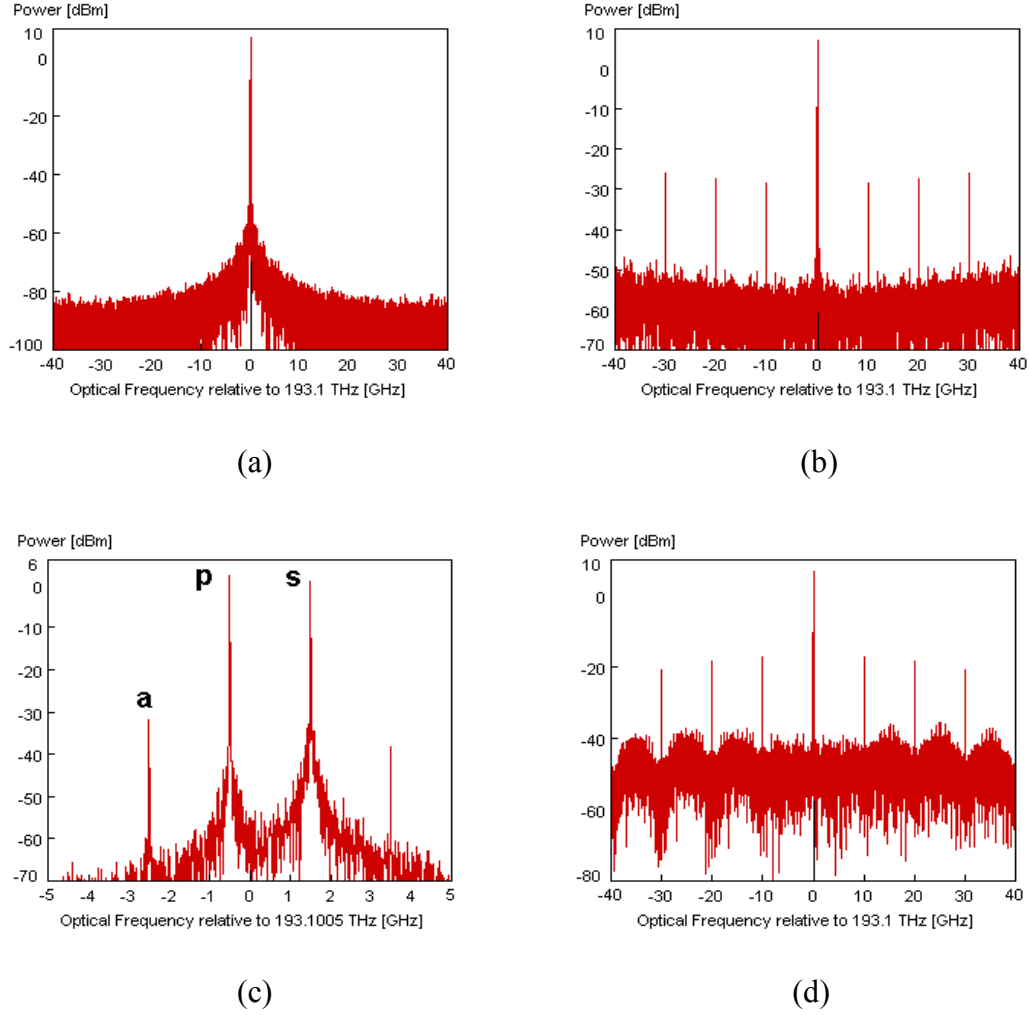
Fig. 3.2. The output optical spectra from NMZI: (a) phase sensitive amplification, CW pump (output signal power = 7.4 dBm); (b) phase sensitive amplification, 10-Gb/s NRZ-BPSK data pump with zero rise time (output signal power = 7.4 dBm); (c) phase insensitive amplification, 10-Gb/s NRZ-BPSK data pump (a: idler, p: pump, s: signal, output signal power = 1 dBm); (d) phase sensitive amplification, 10-Gb/s NRZ-BPSK data pump with rise time of 0.25 bit period (output signal power = 7.1 dBm).

Fig. 3.2(a) and (b) show that there is no difference of the amplified signal power between the

CW pump and the 10-Gb/s NRZ-BPSK data pump as expected. The optical spectral modes at the

harmonics of 10 GHz are due to non-ideal BPSK data, even though the rising time was set to

zero in the VPI photonics simulator. The concave-like background profile is due to the gain

dependence of DFWM on GVD. Fig. 3.2(c) shows the optical spectrum of the signal after phase

insensitive amplification with the CW pump. The output signal power is much smaller compared

to the phase sensitive amplification process. Fig. 3.2(d) shows the case when the pump is10-Gb/s

NRZ-BPSK data as with a rise time of a quarter bit period. The output power was reduced

compared to the case of zero rising time because the gain of the PSA is sensitive to the pumping

phase, however, the output power is still much higher than the case of phase insensitive

amplification.

$E_p(0)$ **PSA** $E_s(L)$

$E_s(0)$
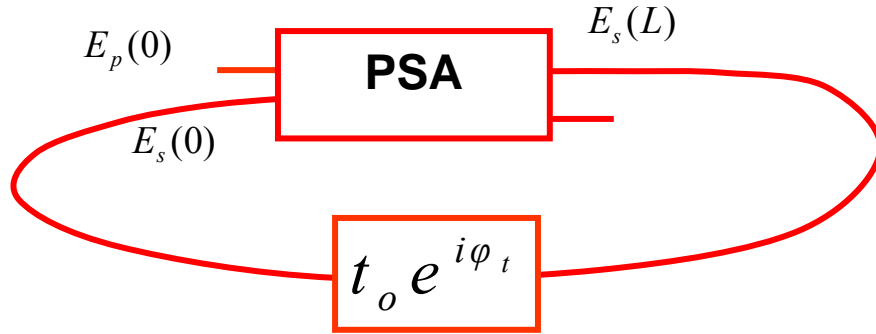
$t_o e^{i\varphi_t}$

Fig. 3.3. Schematic diagram of a PSO. PSA: Phase sensitive amplifier.

3.2.3 Stability analysis of phase sensitive oscillator

Fig. 3.3 shows the schematic diagram of a PSO. The complex transmittance of the oscillator, $t_o e^{i\phi_t}$, is from the output of the PSA to the input of the PSA. The steady state solution should satisfy the following equation for a given pumping power:

$$t_o e^{i\phi_t} = E_s(0)/E_s(L) . \quad (3.9)$$

The relation between, the input, output and pump power of the PSA is given by Eq. (3.1).

A linear stability analysis of a time-discrete system was used to investigate the stability of the PSO [58]. First, the input signal was sampled with respect to the round trip of the cavity as follows: $E_0 = E_s(z=0, t=0)$, $E_1 = E_s(0,\tau)$, $E_2 = E_s(0,2\tau)$ ... where τ is the round trip time.

Let us introduce $x_n = \text{Re}(E_n) = |E_n|\cos(\phi_n)$ and $y_n = \text{Im}(E_n) = |E_n|\sin(\phi_n)$, where ϕ_n is the phase of the signal for the nth round trip.

The time-discrete system can be written as

$$\begin{bmatrix} x_{n+1} \\ y_{n+1} \end{bmatrix} = \begin{bmatrix} f(x_n, y_n) \\ g(x_n, y_n) \end{bmatrix} , \text{where}$$

$$\begin{bmatrix} f(x_n, y_n) \\ g(x_n, y_n) \end{bmatrix} = \begin{bmatrix} -t_o\{y_n \cos(\phi_t + \phi_n)\cos\phi_{NL} + x\sin(\phi_t + \phi_n)\cos\phi_{NL} + \sqrt{P_{p0}}\sin(\phi_t + \phi_n)\sin\phi_{NL}\} \\ t_o\{x_n \cos(\phi_t + \phi_n)\cos\phi_{NL} - y\sin(\phi_t + \phi_n)\cos\phi_{NL} + \sqrt{P_{p0}}\cos(\phi_t + \phi_n)\sin\phi_{NL}\} \end{bmatrix} . \quad (3.10)$$

assuming that the pump phase ϕ_{p0} is set to 0. In this analysis, the phase of the signal, rather than the pump, was a variable parameter.

If (x_0, y_0) is a steady state solution of the system such that $\begin{bmatrix} x_0 \\ y_0 \end{bmatrix} = \begin{bmatrix} f(x_0, y_0) \\ g(x_0, y_0) \end{bmatrix}$, the solution

is stable if the absolute values of the two eigenvalues of the Jacobian

matrix $\begin{bmatrix} f_x(x_0, y_0) & f_y(x_0, y_0) \\ g_x(x_0, y_0) & g_y(x_0, y_0) \end{bmatrix}$ are less than 1. In addition to this stability criterion, it is

required that the gain of phase sensitive amplification is larger than that of the phase insensitive amplification. This assures the gain threshold of the degenerate OPO (or PSO) is smaller than that of the non-degenerate OPO for carrier recovery.

The linear stability analysis introduces a small variation to the steady state solution and we evaluate the small variation to see if it will be diminished in the system. In real system, the pump power, loss, and optical path of cavity are drifting constantly. To find a new steady state solution with the condition that any of the above parameters is changed, we introduce a small perturbation δq to parameter q. The new steady state solution $(x_0 + \delta x_0, y_0 + \delta y_0)$ should satisfy

$$\begin{bmatrix} x_0 + \delta x_0 \\ y_0 + \delta y_0 \end{bmatrix} = \begin{bmatrix} f(x_0 + \delta x, y_0 + \delta y_0; q + \delta q) \\ g(x_0 + \delta x, y_0 + \delta y_0; q + \delta q) \end{bmatrix}.$$

Using a first order approximation, the small variation can be found by

$$\begin{bmatrix} \delta x_0 \\ \delta y_0 \end{bmatrix} = \begin{bmatrix} 1 - f_x(x_0, y_0; q) & -f_y(x_0, y_0; q) \\ -g_x(x_0, y_0; q) & 1 - g_y(x_0, y_0; q) \end{bmatrix}^{-1} \begin{bmatrix} f(x_0, y_0; q) \\ g(x_0, y_0; q) \end{bmatrix} \delta q. \qquad (3.11)$$

An example of the stable steady state solutions is in Fig. 3.4(a). The pump phase was set to 0. The nonlinear coefficient γ was $1200 / \text{km} \cdot \text{W}$ and the length of the nonlinear fiber was 4.4 m. The input signal power and phase were changed to test the stability. The transmittance for the steady state can be found from Eq. (3.9). The stability of the signal was evaluated.
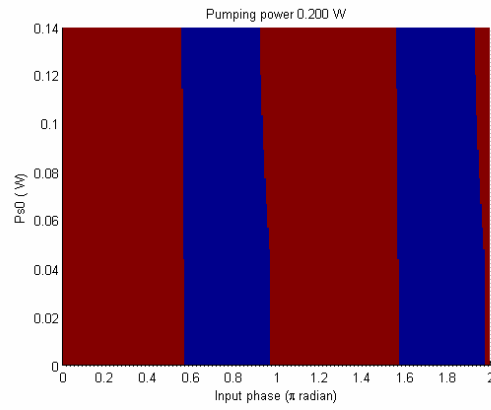
(a)
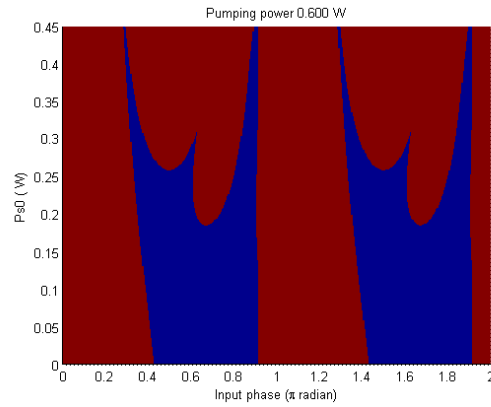
(b)

Fig. 3.4. Stable steady-state regions (colored blue): (a) pump power = 200 mW, (b) pump power = 600 mW.

The blue regions in Fig. 3.4 show the input signals that satisfy stable steady-state conditions. The pump power was set to 200 mW in Fig. 3.4(a) and 600 mW in Fig. 3.4(b). Because of the two-fold symmetry of the pump phase as described, the results also show two-fold symmetry with respect to the input phase. The pump phase was set to zero.
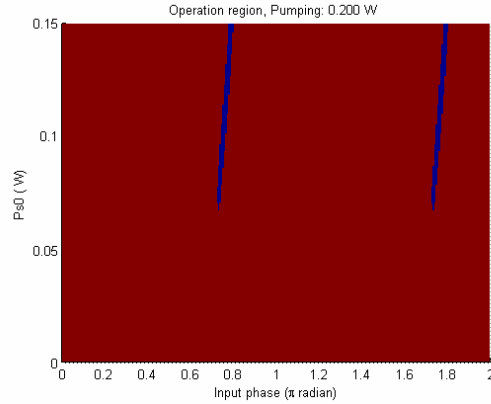
(a)
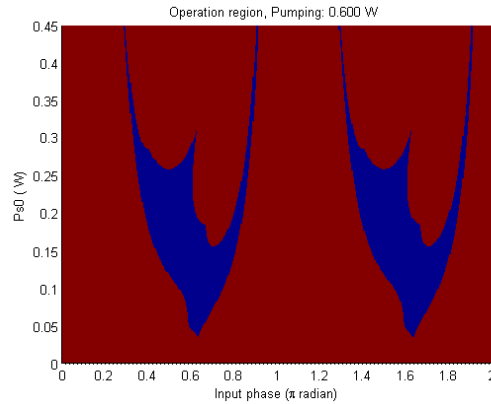
(b)

Fig. 3.5. Blue regions are operating regimes with high perturbation tolerance: (a) pump power = 200 mW, (b) pump power = 600 mW.

It is important to investigate the perturbation tolerance, since a real system requires a feedback controller for stabilization of the output signal against environmental drifts, whose

dynamic range is limited. The operating regime with high tolerance (output power changed less than 5%) to perturbations was determined for the following perturbations: 1 % variation of pump power, 1 % variation of transmission, or 7.2^{o} phase change in optical path. The criterion of 5 % output power variation is arbitrary. The results of the evaluation are shown in Fig. 3.5.

To understand the stability tolerance of the PSO, the phase-dependent gains of the PSA are calculated for the input signal powers and the pump powers. The output signal phase versus input signal phase relative to that of the pump in the PSA was also calculated.

Fig. 3.6(a) shows the calculated phase relations between the input signal and the output signal by the PSA when the pump and the input signal powers are 200 mW and 80 mW, respectively. The phase dependent gain is plotted in Fig. 3.6(b).

(a)   (b)
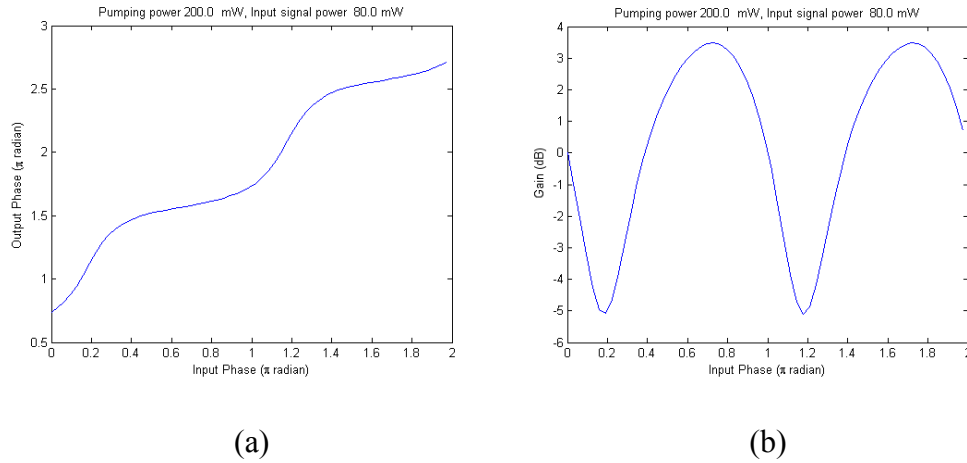
Fig. 3.6. (a) The input phase versus the output phase of the signal. (b) The phase dependent gain (the input phase of the pump was set to zero).
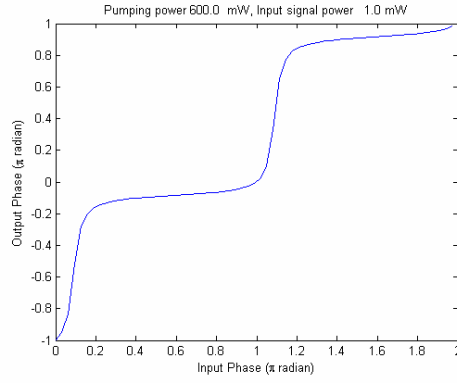
(a)
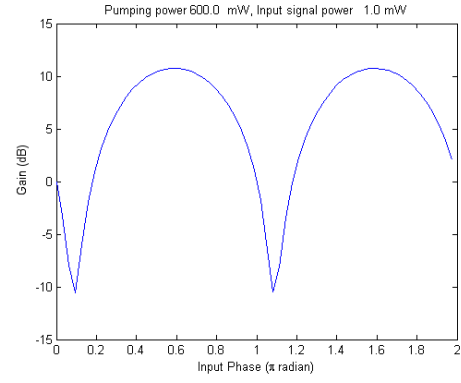
(b)
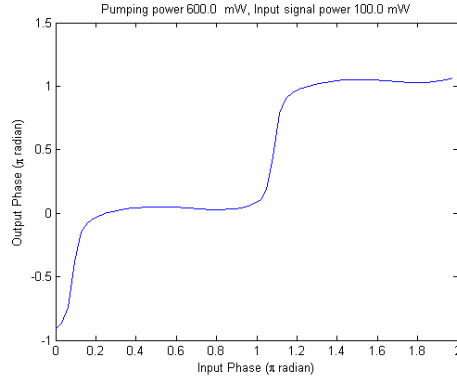
(c)
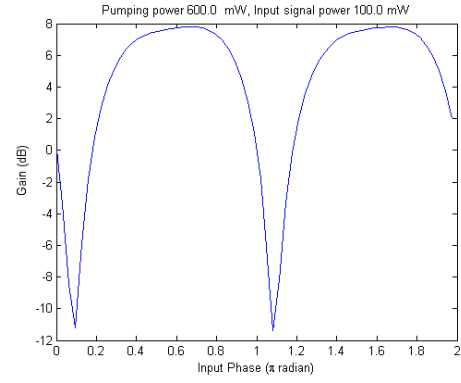
(d)
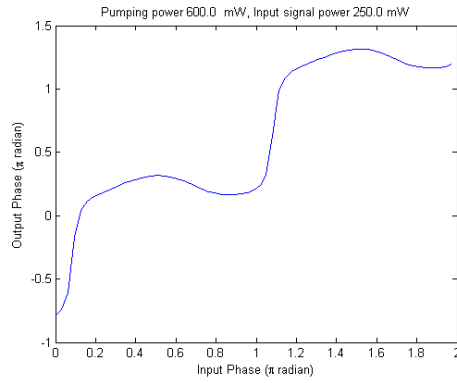
(e)
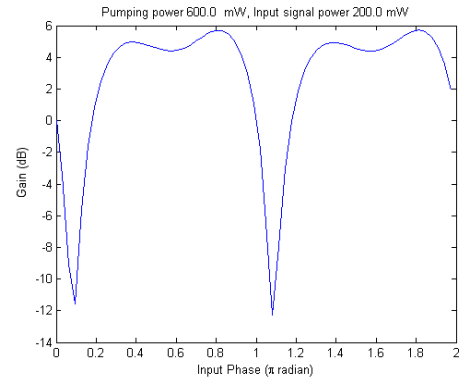
(f)

Fig. 3.7. (a), (c), and (e): The output phase versus the input phase of the signal. (b),(d), and (f): The phase dependent gain (the input phase of the pump was set to zero).

60

Fig. 3.7(a), (c) and (e) show the calculated phase relations between the input signal and the output signal of the PSA as a function of the input signal power when the pump power is 600 mW. Fig. 3.7(b), (d) and (f) show the phase-dependent gain for each case.

The regions of high perturbation tolerance are narrow strips when the pump power is 200 mW. However, these regions are much wider and have a more complicated dependence on the input signal power when the pump power is 600 mW.

The following is the first observation. The output phase dependence on the input phase of the signal is more step-like for the pump power of 600 mW, compared to the case of 200 mW. That means the variation of the output phase can be limited in a certain range for some range of the input phase of the signal. This provides the phase regeneration capability of the PSA [57].

The second observation is from the case of the pump power of 600 mW. Fig. 3.7 (b) does not show gain depletion with the input signal power of 1 mW. For this case, there is no input signal phase that can have high perturbation tolerance according to Fig. 3.5(b). Fig. 3.7(d) shows the gain depletion with the input signal power of 100 mW. For this case, the PSO can have high perturbation tolerance for a wide range of the input signal phase. Fig. 3.7(f) shows the split of the gain peak due to gain depletion with the input signal power of 250 mW. For this case, the stable operation regions are also split. The input signal phase providing high perturbation tolerance can be found near the peaks of the gain depletion. That means the output power is less dependent on the input signal phase or power.

In conclusion, the PSO can have high perturbation tolerance when the output signal phase and power from the PSA do not highly depend on the input signal phase and power.
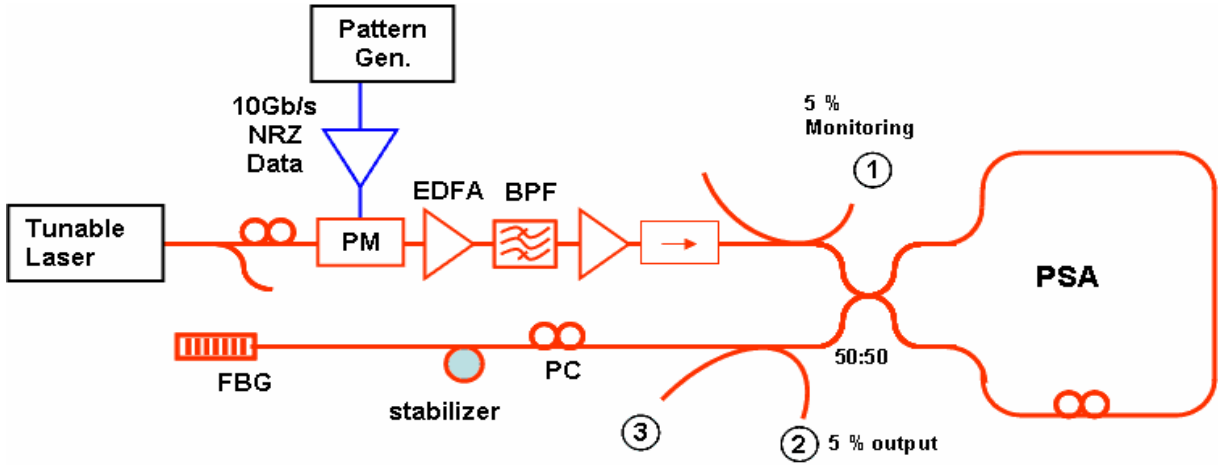
Fig. 3.8. Experimental setup. PC: polarization controller, PM: Phase modulator, BPF: bandpass filter, FBG: fiber Bragg gratings, PSA: phase sensitive amplifier.

3.2.4 Experimental setup and results

Fig. 3.8 shows the experimental setup of PSO. Bi-NLF(bismuth-oxide-based nonlinear fiber) was used for PSA. The nonlinear coefficient γ was about 1200/kmW and the effective length was about 4.4 m. UHNA fiber (ultra-high numerical aperture fiber) was spliced between Bi-NLF and standard single mode fiber SMF28. NOLM was used for better stability of PSA instead of NMZI. The cavity was formed by using a fiber Bragg grating (FBG) as the end mirror. The 3-dB bandwidth of FBG is 3.3 GHz. The total length of the cavity including PSA is less than 20 m. The insertion loss of the PSA was about 7 dB. Port ① and ② from 5 % couplers were used to monitor the pump and the recovered carrier respectively. Stabilization was achieved using a fiber stretcher by monitoring the output power at port ②.
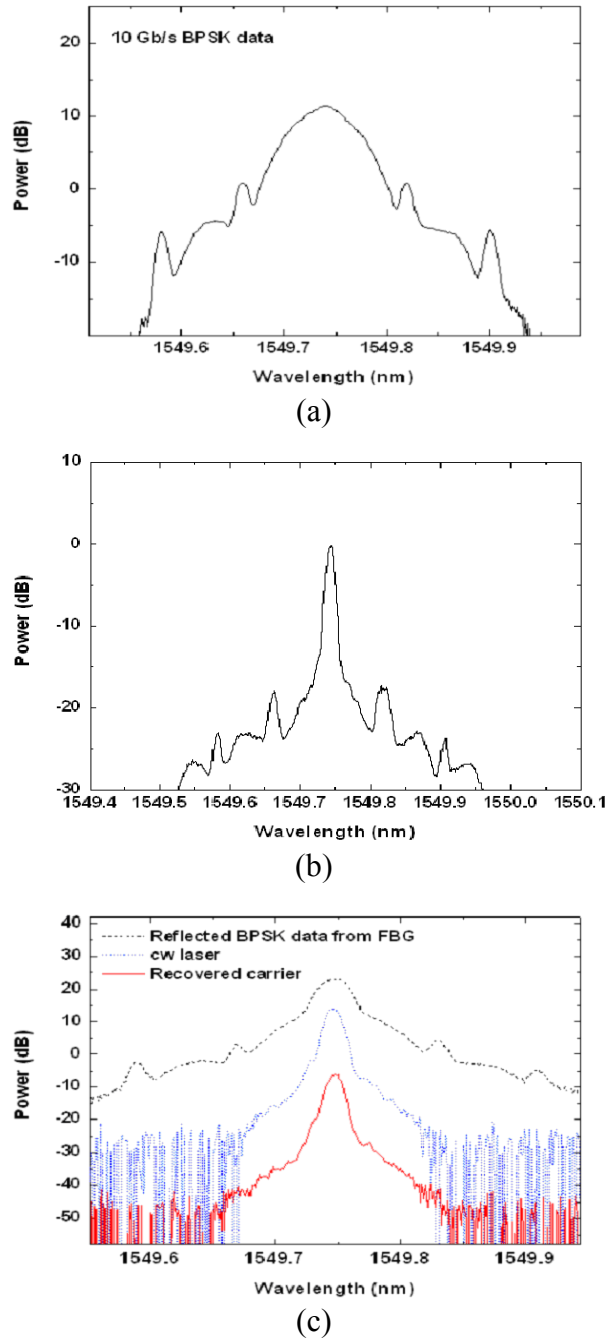
Fig. 3.9. Optical spectra of (a) 10-Gb/s BPSK data, (b) recovered carrier with data leaking (c) recovered carrier, transmitter laser, and reflected BPSK data from FBG without OPO (Resolution bandwidth = 0.01 nm).

A pseudo-random 10-Gb/s BPSK signal of length 2^{15}-1 with an average power of 2 W was used as the pump. The optical spectrum of the pump is shown in Fig. 3.9(a), which does not have the optical carrier component as expected. Fig. 3.9(b) shows the optical spectra observed at port ③ , which shows the recovered optical carrier with leaking data from PSA caused by imperfect NOLM. This optical spectrum is clearly different from that of the pump. Fig. 3.9(c) shows the optical spectra of transmitter laser (CW), the recovered optical carrier, and the 10-Gb/s BPSK signal reflected from the FBG but without the cavity. The spectral profile of the recovered optical carrier is clearly closer to that of transmitter laser than that of the reflected BPSK signal. However, it was not clear if the recovered carrier had other optical components due to non-degenerate OPO.

To verify that optical carrier phase recovery was indeed achieved, the RF spectra of optical heterodyned signals were measured. Fig. 3.10 shows the RF spectra of the optical heterodyne signal between the transmitter laser (a), the BPSK signal (b) as well as the recovered carrier (c) and the transmitter laser frequency shifted by 100 MHz using an AO modulator. In Fig. 3.10(b), the noise profile of the transmitter laser was masked by the spectral components from data modulation. The residual carrier tone was due to chirp generated by finite rising time of NRZ-BPSK data. However, in Fig. 3.10(c), spectral components due to data modulation have been suppressed revealing the noise profile of the laser almost identical to that of the self-heterodyne spectrum of the transmitter laser in Fig. 3.10(a). This clearly indicates successful all-optical carrier recovery using the phase sensitive oscillator.
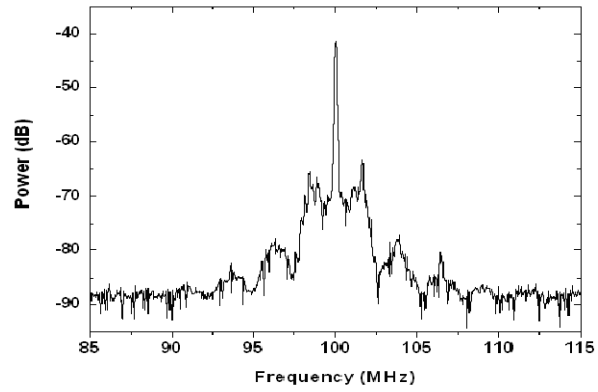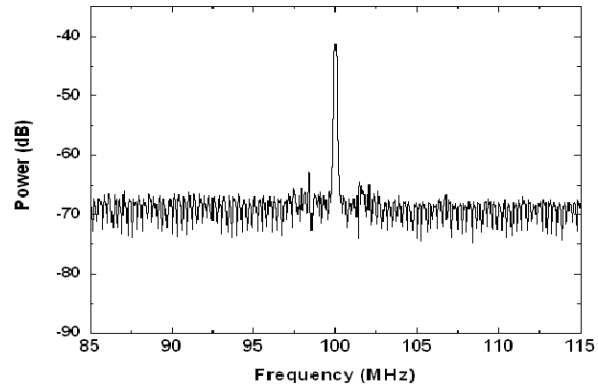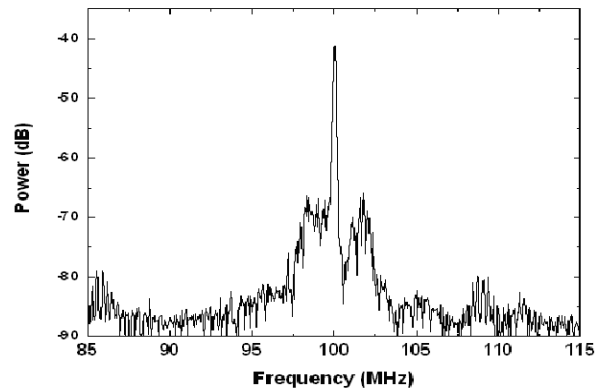
Fig. 3.10. RF spectra of heterodyne signal between (a) the transmitter laser (self-heterodyne with ~ 80-m delay), (b) BPSK signal, (c) recovered optical carrier and the transmitter laser frequency shifted by 100 MHz (resolution bandwidth = 100 kHz).

Fig. 3.11 shows the eye diagram of the homodyne demodulated 10-Gb/s NRZ BPSK data using the recovered carrier. The relatively large eye opening demonstrates the feasibility of carrier synchronization using PSO.

20 ps/div
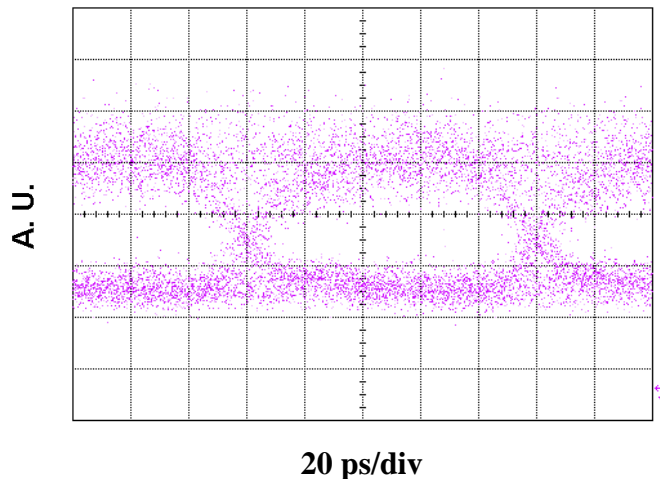
Fig. 3.11. Eye diagram of the homodyne demodulated 10-Gb/s NRZ BPSK data.

3.2.5 Summary

We proposed and analyzed, for the first time, an all-optical carrier synchronization (carrier phase and polarization recovery) scheme using a PSO which adopted PSA as a gain block. The gain of PSA is phase and polarization sensitive. The study showed that the small signal gain of the phase sensitive amplification was much larger than that of the phase insensitive amplification. The CW carrier signal can be amplified by PSA with either a CW pump or a BPSK pump. As a result, an optical carrier with the same polarization and phase as the pump oscillates in a PSO when it is pumped with a BPSK signal.

All-optical carrier synchronization from 10-Gb/s BPSK data was demonstrated in experiment. This can be used for all-optical regeneration of PSK signal which requires a recovered carrier in terms of phase and polarization.

CHAPTER 4: CHARACTERIZATION OF OPTICAL DATA IN ADVANCED OPTICAL COMMUNICATION

4.1 Introduction

Recently, linear optical sampling based on the interferometric technique was proposed which enables the full characterization of the optical data by measuring the phase and amplitude at the same time with high sensitivity.

Section 4.2 studies on requirements for the sampling source in coherent linear sampling source. In section 4.3, complex constellation diagram measurement for optical communications is presented

4.2 Linear optical sampling and requirements

4.2.1 Introduction

Techniques for the measurement of high-speed temporal waveforms have advanced in response to demand in optical communication systems where per-channel data rate has approached 160 Gb/s and beyond. Traditional electronic measurement techniques using sample-and-hold circuits have given way to nonlinear optical sampling techniques [35, 59-62].

In nonlinear optical sampling higher temporal resolution is achieved because a short optical pulse provides the gating function. Eye diagram measurement up to 500 Gb/s has been demonstrated [63]. This approach suffers from poor sensitivity because of the inherent low efficiency of nonlinear optical mixing.

Recently, a new approach to optical waveform measurement based on coherent homodyne linear optical sampling has been demonstrated. Since ultra-short optical pulses are used in coherent linear optical sampling, it also provides high temporal resolution. Eye diagram measurement up to 640 Gb/s has been demonstrated [12]. Because coherent homodyne sampling is a linear process, measurement sensitivity ($3 \cdot 10^3 \, \mathrm{mW}^2$), three orders of magnitude better than nonlinear optical techniques ($10^6 \, \mathrm{mW}^2$), is possible [12].

Furthermore, coherent linear optical sampling offers the capability of measuring both the intensity and phase of optical signals, providing a timely diagnostic tool for investigating advanced modulation formats such as differential (quadrature) phase shift keying (DPSK/DQPSK) [64, 65] before and after amplified fiber transmission where transmission impairments such as amplified spontaneous emission (ASE) can accumulated. In reference [65], the constellation diagram of DPSK signals at 10 Gb/s and 40 Gb/s was measured experimentally. A deterministic rotation of the constellation diagram was observed and attributed to carrier-envelope offset (CEO) of the mode-locked laser.

In this section, we analyze the coherent linear sampling process and point out the actual mechanism for the rotation of the constellation diagram. In addition, we establish the requirements for the sampling pulses to eliminate this rotation and to achieve desired measurement accuracy for the phase and envelope profile.

4.2.2 Analysis of linear optical sampling

The schematic diagram of linear optical sampling is shown in Fig. 4.1(a). The phase and intensity of the optical data signal, $E_d(t)$, are measured by observing its interference with two

orthogonal quadratures of the sampling pulse, $E_s(t)$. In the upper branch, the balanced detectors measure the interference of the data signal and sampling pulse $\mathrm{Re}[E_s(t)^* E_d(t)]$. The sampling pulse is delayed in phase by $\pi/2$ before interfering with the data signal in the lower branch. The balanced detectors in the lower branch therefore measure the interference signal $\mathrm{Re}[\{E_s(t)e^{i\pi/2}\}^* E_d(t)] = \mathrm{Im}[E_s(t)^* E_d(t)]$. Therefore, the quadrature interference signals in the two branches together determine the complex quantity $E_s(t)^* E_d(t)$ completely (except a proportionality constant).
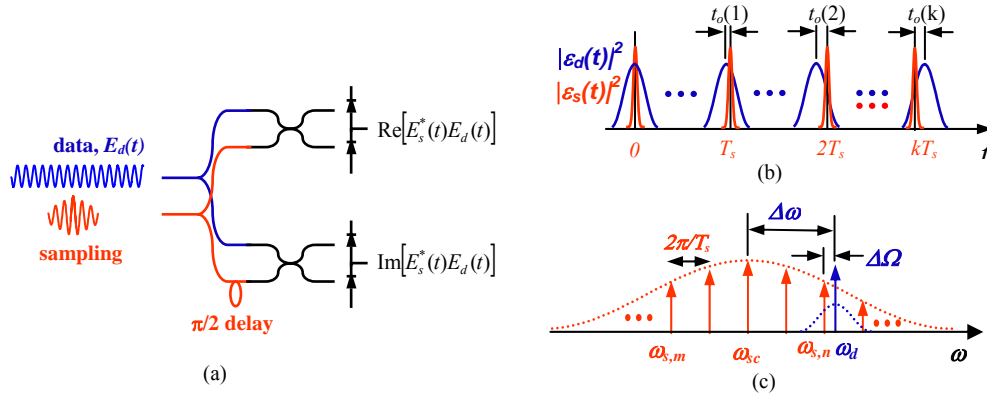
Fig. 4.1. (a) Schematic diagram of the linear optical sampling. Data and sampling pulses have the same polarization. (b) Walk off in the time domain between the sampling pulse (narrow) and data pulse (broad). (c) Schematic of the optical spectra of the data and sampling source: (ω_{sc} is the center frequency of the sampling source, ω_d is the optical carrier frequency of the data signal, $\Delta\Omega$, called carrier frequency offset, is the offset of the optical carrier of the data signal from the closest mode of the sampling source, and $\Delta\omega$, called carrier frequency detuning, is the detuning of the optical carrier of the data signal from the center frequency of the sampling source).

High temporal resolution can be achieved even with low speed detectors by using a short sampling pulse, for example, from a mode-locked laser, which functions essentially as a gated local oscillator of coherent detection [12, 65]. The interference between the data signal and sampling pulse occurs only during this gated duration.

The electric field of the mode-locked sampling pulse, $E_s(t)$, can be expressed as

$$E_s(t) = \sum_m a_m e^{i(\omega_{s,m}t+\phi_m)}, \quad \text{with } \omega_{s,m} = \frac{2\pi m}{T_s} + \alpha \,, \tag{4.1}$$

where $\omega_{s,m}$ is the angular frequency of the mode, T_s is the period of the sampling pulse, a_m and ϕ_m are the amplitude and phase of the m_{th} mode. The parameter $0 < \alpha < 2\pi/T_s$ is a frequency offset that describes the CEO [66]. It is straightforward to verify that a nonzero offset leads to pulse-to-pulse relative shifts between the pulse envelope and the optical carrier.

The sampling pulse train can also be decomposed into a slowly varying envelope around an optical carrier of center frequency $\omega_{sc} = 2\pi n_0/T_s$ as

$$E_s(t) = \left\{ \sum_m a_m e^{i((\omega_{s,m}-\omega_{sc})t+\phi_m)} \right\} e^{i\omega_{sc}t} = \left\{ \sum_m a_m e^{i(\frac{2\pi(m-m_0)}{T_s}t+\phi_m)} \right\} e^{i\omega_{sc}t}. \tag{4.2}$$

As expected, the slowly-varying envelope (the summation in the brackets) is periodic with period T_s. The above expression can be rewritten by introducing a complex envelope function $\varepsilon_s(t)$ for a single pulse as

$$E_s(t) = \sum_l \varepsilon_s(t - lT_s) e^{i\omega_{sc}t}. \tag{4.3}$$

71

For simplicity, let's assume that data pulse train is also periodic, for the time being, with a period T_d, given by

$$E_d(t) = \sum_l \varepsilon_d(t - lT_d) e^{i(\omega_d t + \phi_{do})} ,$$

(4.4)

where $\varepsilon_d(t)$ is the slowly-varying complex envelope profile for a single pulse, ω_d is the carrier frequency, ϕ_{do} is a constant initial phase, and T_d is the period of the data pulse.

When one is interested in measuring the constellation diagram of the data signals, the period of the sampling pulse is chosen to be exactly equal to the proper integer multiple of the period of the data signal. On the other hand, when one is interested in measuring the complex (intensity and phase) envelope of the data, it is convenient to make the period of the sampling pulses intentionally deviate slightly from an integer multiple of the period of the data signal so that successive sampling pulses sample the data pulses at different locations as shown in Fig. 4.1(b). When we assume that the peaks of the data pulse and the sampling pulse are aligned at $t = 0$ in Fig. 4.1(b), the off-set, $t_o(k)$, for the k_{th} sampling pulse is given by $t_o(k) = [(kT_s + 0.5T_d) \bmod T_d] - 0.5T_d$ where mod is the modulus function.

With the above notations, the measured complex envelope by the k_{th} sampling pulse can be expressed as

$$\chi(k) = \int_{(k-0.5)T_s}^{(k+0.5)T_s} E_s(t)^* E_d(t) dt$$

(4.5)

$$= \int_{(k-0.5)T_s}^{(k+0.5)T_s} \varepsilon_s(t - kT_s)^* \varepsilon_d(t - kT_s + t_o(k)) e^{i((\omega_d - \omega_{sc})t + \phi_{do})} dt,$$

where the integration is due to the slow detector. Now let's assume that the carrier frequency of the data signal falls within the spectrum of mode-locked laser at an arbitrary position near one of the modes as shown on the Fig. 4.1(c) so that $\omega_d = \omega_{s,n} + \Delta\Omega$, where $\Delta\Omega$ is the carrier frequency offset. Then Eq. (4.5) becomes

$$\chi(k) = \int_{(k-0.5)T_s}^{(k+0.5)T_s} \varepsilon_s(t - kT_s)^* \varepsilon_d(t - kT_s + t_o(k)) e^{i((\omega_{s,n} - \omega_{sc})t + \Delta\Omega t + \phi_{do})} \, dt$$

$$= e^{i\phi_{do}} \int_{-0.5T_s}^{0.5T_s} \varepsilon_s(t')^* \varepsilon_d(t' + t_o(k)) e^{i\left[\frac{2\pi(n - m_0)}{T_s} t'\right]} e^{i\Delta\Omega(t' + kT_s)} \, dt' \tag{4.6}$$

$$= e^{i\phi_{do}} e^{i\Delta\Omega kT_s} \int_{-0.5T_s}^{0.5T_s} \varepsilon_s(t')^* \varepsilon_d(t' + t_o(k)) e^{i\Delta\omega t'} \, dt',$$

where we have used the fact that $\exp\left\{i\frac{2\pi(n - m_0)}{T_s} kT_s\right\} = 1$ and $\Delta\omega = \omega_d - \omega_{sc}$ is the carrier frequency detuning between the carrier frequencies.

Let's assume that the sampling pulsewidth (Δt_s, FWHM) is much smaller than the pulsewidth (Δt_d) of the data signal so that the envelope and phase of the data pulse are almost constant during sampling. Then Eq. (4.6) becomes

$$\chi(k) \approx \varepsilon_d(t_o(k)) e^{i\phi_{do}} e^{i\Delta\Omega kT_s} \int_{-\infty}^{\infty} \varepsilon_s(t')^* e^{i\Delta\omega t'} \, dt' \quad (\text{for } \Delta t_s \ll \Delta t_d)$$

$$\tag{4.7}$$

$$= \varepsilon_d(t_o(k)) e^{i\phi_{do}} \tilde{\varepsilon}_s(\Delta\omega)^* e^{i\Delta\Omega kT_s},$$

where $\widetilde{\varepsilon}_s(\omega)$ is the Fourier transformation of the slowly varying envelope $\varepsilon_s(t)$. Eq. (4.7) is the main results of the analysis of the linear optical sampling process. There are several important conclusions that can be derived from Eq. (4.7).

First, the CEO does not play any role in the measurement of the complex envelope of the data signal. This is because linear sampling is proportional to the interference between the optical carriers, integrated over the sampling pulse. This interference signal depends on the optical carrier frequency detuning only and is independent of CEO. This is clear as the parameter α is absent from Eq. (4.7).

Second, when there is a carrier frequency offset, there will be a deterministic phase error for the measured signal. Consider the special case when the data pulses are uniform and the sampling pulse period is an integer multiple of the period of the data pulses. When the carrier frequency offset is zero, $\Delta\Omega = 0$, the measurement will yield an identical results for every sampling pulse as it should be as shown in Fig. 4.2(a). However, when $\Delta\Omega \neq 0$, the measurement will yield a different result for each sampling pulse which is rotated by phase angle of $\Delta\Omega T_S$ between successive sampling pulses, as shown in Fig. 4.2(b). It should be pointed out that the magnitude of the data signal will not be affected by this misalignment. The constellation diagram can be obtained without this deterministic rotation of phase by locking one of the modes of mode-locked laser to the optical carrier of the data signal. The periodic interference pattern between a mode-locked laser and a CW laser has been observed when one of the modes of the mode-locked laser is locked to the CW laser [67]. This rotation of the measured phase can potentially be corrected using a proper software correction scheme [65], assuming that the frequencies of the data signal and the sampling source stay fixed during measurement.

74

Third, the measured intensity ($\propto |\chi(k)|^2$) will be proportional to the spectral power density of the sampling pulse at the carrier frequency of the data signal as shown in Eq. (4.7). A quantitative example is given in Section 4.2.3 for the case of Gaussian pulses. This dependence of the measured intensity on the carrier frequency of the data signal should be taken into consideration when comparing measured results of different wavelength-division multiplexed (WDM) channels using the same sampling source.
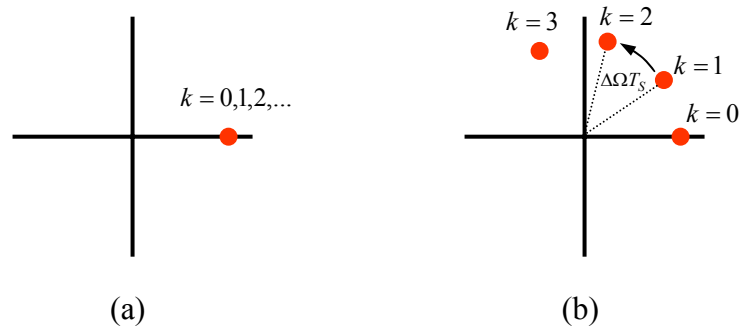
Fig. 4.2. Constellation diagram when the data phase is constant, (a) $\Delta\Omega = 0$ and (b) $\Delta\Omega \neq 0$.

4.2.3 Effects of chirp and finite pulsewidth of the sampling source

In this section, we describe the effects of the finite pulsewidth and linear chirp of the sampling pulses on the measurement of the complex envelope by retaining perturbation terms up to $(\Delta t_s / \Delta t_d)^2$, which were ignored in Eq. (4.7). As an example, we consider the case of Gaussian pulses for both sampling pulses and data pulses. The slowly varying envelope of the Gaussian sampling pulse is

$$\varepsilon_s(t) = \varepsilon_{s0} \frac{e^{-(1+iC)(2\ln 2\, t^2 / \Delta t_s^2)}}{\sqrt{\dfrac{\sqrt{\pi}\,\Delta t_s}{2\sqrt{\ln 2}}}} \quad , \tag{4.8}$$

where C is the chirp parameter of the sampling pulse and the energy of a pulse is $|\varepsilon_{s0}|^2$. The

data pulses are also Gaussian but with no chirp. Let's assume that one of the modes of the mode-

locked laser is locked to the optical carrier of the data signal so that $\Delta\Omega = 0$ in Eq. (4.6).

It is straightforward to show that if the sampling pulsewidth is much smaller compared to the

pulsewidth of the data signal, the measured pulsewidth is

$$\Delta t_d' \approx \Delta t_d \left[1 + \frac{1}{2(1+C^2)} \left(\frac{\Delta t_s}{\Delta t_d} \right)^2 \right], \qquad (\Delta t_s^2 \ll \Delta t_d^2) \tag{4.9a}$$

$$= \Delta t_d \left[1 + \frac{8(\ln 2)^2}{\Delta t_d^2 \Delta\omega_s^2} \right], \qquad (\Delta t_s = \frac{4\ln 2\sqrt{1+C^2}}{\Delta\omega_s}), \tag{4.9b}$$

where $\Delta\omega_s$ is the spectral bandwidth (FWHM) of the sampling pulse. Eq. (4.9b) shows that the

broadening of measured pulsewidth, $\Delta t_d' - \Delta t_d$, is inversely proportional to the square of the

spectral bandwidth of sampling pulse and the pulsewidth of the data signal. For a fixed spectral

bandwidth, chirp of the sampling source doesn't affect the measurement result. On the other

hand, Eq. (4.9a) indicates that, for a fixed sampling pulsewidth, as chirp of the sampling pulse

increases (bandwidth increases), the error in the measurement decreases. This is because the

interference signals at the leading edge and trailing edge of the sampling pulse oscillate in time

due to chirp. When integrated with a slow detector, the oscillating interference signals average to zero effectively narrowing the sampling pulsewidth.

As mentioned in the previous section, the intensity ($\propto |\chi(k)|^2$) of the complex envelope is proportional to the spectral power density of the sampling pulse at the carrier frequency of the data signal. For the Gaussian pulses considered here, the measured intensity is proportional to

$$\frac{|\varepsilon_{s0}|^2}{\Delta\omega_s} e^{-(4\ln 2)(\frac{\Delta\omega}{\Delta\omega_s})^2} \qquad (\Delta t_s^{\,2} << \Delta t_d^{\,2}), \qquad\qquad (4.10)$$

when a carrier frequency of the data signal is detuned from the center frequency of the Gaussian sampling pulse. A carrier frequency detuning of about $0.2\Delta\omega_s$ leads to a 10% reduction in measured intensity.

Assuming that the sampling pulsewidth is much smaller than that of the data signal, the measured phase error $\Phi(t_o(k))$ can be calculated from the phase of $\chi(k)$ in Eq. (4.6):

$$\Phi(t_o) \approx \frac{2\ln 2\, C\, \Delta t_s^{\,2} t_o^{\,2} / \Delta t_d^{\,2} - \Delta\omega\, t_o \Delta t_s^{\,2}}{(1 + C^2)\, \Delta t_d^{\,2}}, \qquad (\Delta t_s^{\,2} << \Delta t_d^{\,2}, t_o < \Delta t_d / 2)$$

$$\qquad\qquad\qquad\qquad\qquad\qquad\qquad\qquad\qquad\qquad\qquad\qquad (4.11)$$

$$= \frac{32(\ln 2)^3\, C\, t_o^{\,2} / \Delta t_d^{\,2} - 16(\ln 2)^2\, \Delta\omega\, t_o}{\Delta\omega_s^{\,2} \Delta t_d^{\,2}} .$$

The first term describes the quadratic phase measurement error due to chirp and the second term describes the linear phase measurement error due to carrier frequency detuning.
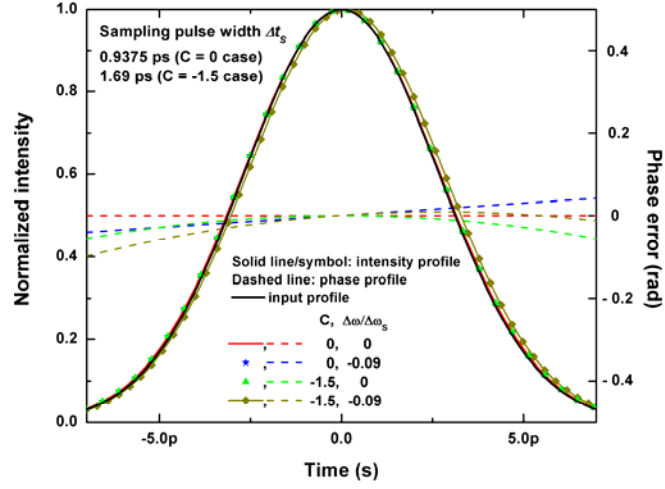
(a)
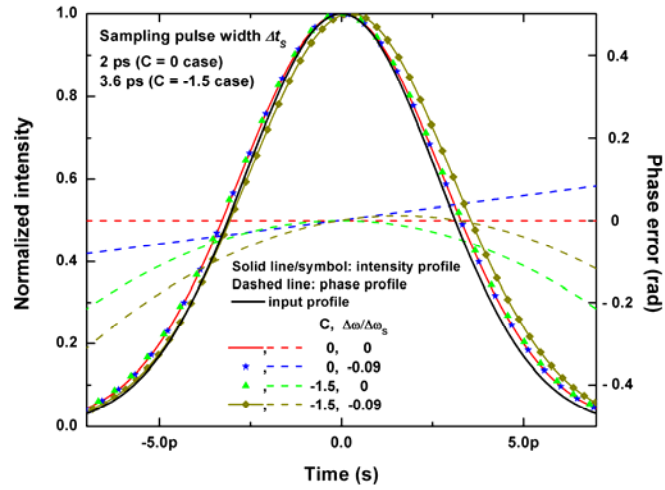
(b)

Fig. 4.3. Numerical simulation of measurement of the envelope profile and phase with linear optical sampling. The sampling pulse bandwidths are 3.769 nm (a) and 1.767 nm (b).

Numerical simulation was performed to confirm the analytic results presented above. The pulsewidth of the data signal was set to be 6.25 ps. The data pulse doesn't have any chirp and the phase was constant. The peaks of the envelope were normalized to unit value to compare the envelope profiles. The chirp of the sampling pulse and optical carrier frequency detuning were varied while the energy of the sampling pulse was fixed in the simulation. Two spectral bandwidths at 3.769 nm (Fig. 4.3(a)) and 1.767 nm (Fig. 4.3(b)) were used. For Fig. 4.3(a), the sampling pulsewidth was 0.9375 ps with no chirp, which is much smaller than the data pulsewidth and thus the analytical results of the previous section apply. The results of numerical simulation agree well with analytical results. For example, pulsewidth broadening was 69.9 fs and 70.3 fs , respectively, using numerical simulation and Eq. (4.9). The phase variations within the pulsewidth of the data signal were 0.011 radian with chirp only, 0.037 radian with detuning only, and 0.038 radian with both chirp and detuning.

For Fig 3(b), the sampling pulsewidth was 2 ps when there was no chirp and 3.6 ps when $C = -1.5$. The normalized carrier frequency detuning, $\Delta\omega/\Delta\omega_s$, was set to either zero or 0.09. Even though the sampling pulsewidth was large compared with that of the data pulse, the qualitative features predicted analytically remain valid. For the parameters chosen, the measured data pulse was broadened by only 5% even though the ratio of sampling pulsewidth to data pulsewidth is rather large. A temporal shift of the intensity profile was observed when there were both carrier frequency detuning and chirp in the sampling source. The phase variations within the pulsewidth of the data signal were 0.048 radian with chirp only, 0.074 radian with detuning only, and 0.095 radian with both chirp and detuning. Comparing the two chirp-only cases, it is verified that the phase error was reduced with increased sampling pulse bandwidth. In practice, linear chirp in the source can easily be compensated. The example here indicates that

high-order chirp, which cannot be easily compensated, will result in phase measurement error. Simulation results for other pulse envelope profiles (such as raised cosine) agree qualitatively with the case for Gaussian pulses.

4.2.4. Summary

In conclusion, we have analyzed the coherent linear optical sampling process. It is found that the measured intensity is proportional to the spectral power density of the sampling pulse at the carrier frequency of the data signal. Carrier frequency offset of the sampling source does not affect intensity measurement. Carrier frequency detuning results in a decrease in the measured intensity. Furthermore, in combination with chirp, carrier frequency detuning will lead to a temporal shift of the intensity profile.

Reliable phase measurement requires carrier synchronization. That means one of the modes of the sampling source be locked to the optical carrier of the data signal. Carrier frequency offset leads to a deterministic rotation of the phase angle between successive sampling periods for the constellation diagram measurement. Carrier frequency detuning (linear chirp) results in a linear (quadratic) phase error in the measurement of the complex envelope for Gaussian sampling pulses. Therefore it is very desirable to lock one of the modes of the mode-locked source to the carrier frequency of the data to remove carrier frequency offset. This has the added benefit of reducing the phase measurement error caused by random phase noise of the sampling source as briefly discussed below.

Linear chirp should be compensated and high-order chirp should be minimized in the sampling source to reduce the phase measurement error. The sampling pulse width should be

sufficiently small ($\Delta t_s / \Delta t_d < 0.2$) to ensure negligible broadening and temporal shift of the measured intensity profile.

4.3 Measurement of complex constellation diagram

4.3.1 Introduction

Linear optical sampling required a low jitter mode-locked laser with a well controlled repetition rate for sampling. Since the carrier frequencies of the mode-locked laser and the measured signal are independent, it required post processing to get phase information by eliminating phase drift caused by heterodyne detection [13, 14, 68]. Even though the linear phase drifts due to carrier frequency offset can be corrected and the random phase drifts due to the finite linewidth of laser can be averaged out by multiple sampling on periodic signals, the numbers of consecutive sampling points are limited by the coherence time of the sources [13].

Assuming the beating linewidth of two lasers (signal source and sampling laser) is $\Delta \nu$ then the variance of the phase difference of the first sampled point and the last sampled point is given by $<\Delta\phi^2> = 2\pi\Delta\nu\tau$ for the sampling duration τ [69]. When it is larger than π^2, the random phase drift can not be removed by averaging for BPSK signal, since there is no way of distinguishing between data '0' and 'π'. For example, the sampling duration is expected to be limited by 157 ns for 10 MHz of beating linewidth of lasers. Assume 1000 sampling points are required to make a constellation diagram to characterize the transmission system then the rate of the sampling pulses should be at least 6.4 GHz.

81

A CW local oscillator could be used instead of ultra-short optical sampling pulses for the characterization of the optical signal if the bit rate and the chirp of interest are in the bandwidth of the measurement system. This relaxes some constraints of using ultra-short sampling pulses such as wavelength tuning, controlling of the sampling pulse rate, timing jitter, and amplitude jitter. Moreover, post processing for the elimination of the phase-drift is not required since the CW local oscillator, which has the same optical carrier as that of the optical signal, is available in a laboratory environment, though it requires stabilization (carrier synchronization) for the homodyne process. The restriction on the linewidth of lasers and sampling duration is removed since it uses the same laser sources for optical signal and local oscillator for homodyne detection.

The constellation diagram and chirp of a 10-Gb/s RZ-BPSK (Return to Zero Binary Phase Shift Key) signal have been measured using a 90° optical hybrid with a CW local oscillator. Constellation diagrams were measured with (and without) added periodic phase noise and amplitude noise. The RZ-BPSK signal was also monitored before and after transmission through 6 km of HNLF (Highly Nonlinear Fiber) showing the development of chirp due to self-phase modulation. Carrier synchronization between the local oscillator and the RZ-BPSK signal was achieved by monitoring 10 GHz clock power from one of the output channels of the optical hybrid. This method does not require any pilot tone or dithering signal or decision circuit for feedback control [33, 37, 38].

4.3.2 Experimental setup

The experimental setup is shown in Fig. 4.4. A single laser source is shared for the local oscillator and the optical data. The 10-Gb/s RZ-BPSK signal was generated using a phase

modulator driven by NRZ data and an amplitude modulator driven by clock signal from the pattern generator. The length of the PRBS was 2^{11} -1. An additional phase modulator and an amplitude modulator following the EDFA and the bandpass filter were used for adding periodic phase and amplitude noise on the optical data. The added phase noise and amplitude noise frequencies were 3.125 GHz and 195.312 MHz respectively. The power of the local oscillator was about 12 dBm and the power of the optical data was around 0 - 3 dBm.
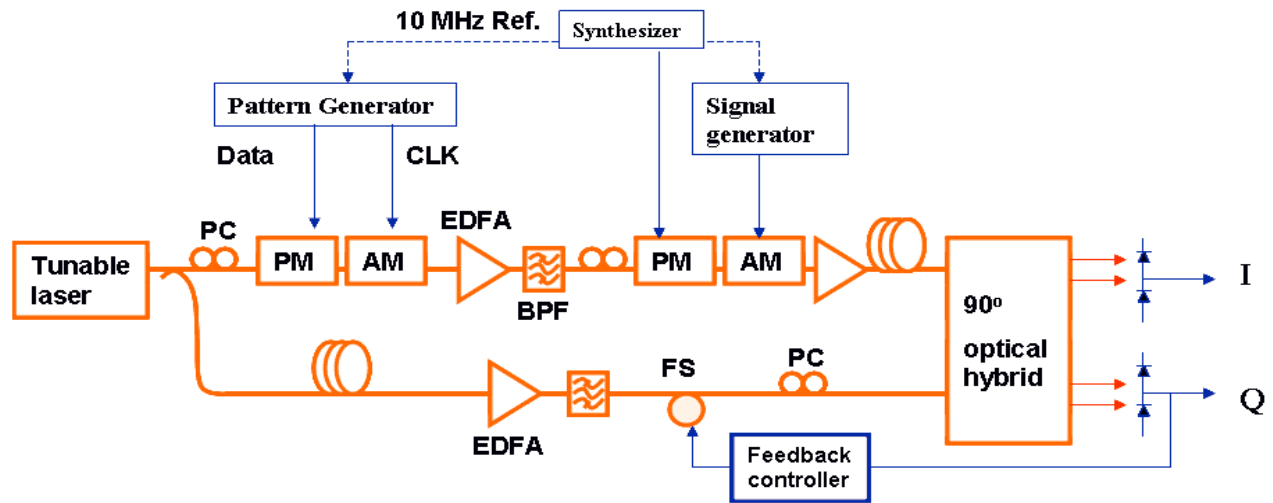
Fig. 4.4. Experimental setup. PM: Phase modulator, AM: Amplitude modulator, FS: Fiber stretcher, BPF: Band pass filter, PC: Polarization controller, EDFA: Erbium-doped fiber amplifier.

The pattern generator, synthesizer and signal generator were synchronized by a 10 MHz reference signal to observe the deterministic error due to the added noise with sampling scope. The optical signal from the tunable laser (Agilent 81633A) was amplified by EDFA and used for local oscillator. The 90° optical hybrid was used for measurement of the *I* (in-phase) and *Q* (quadrature-phase) signals used for measurement of the electric field as described in the following subsection. The bandwidth of the photo-detectors and the sampling scope were above 40 GHz. The time delays of the local oscillator and optical data from the splitter to the optical hybrid were measured and matched to the order of nanosecond. And a stabilizer based on fiber stretcher was used for homodyne detection.
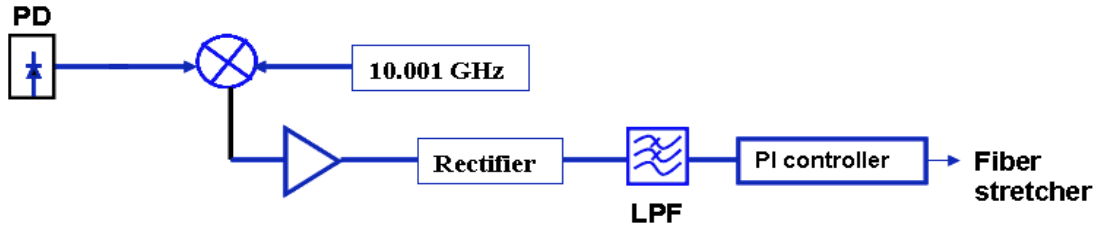
Fig. 4.5. Schematic diagram of the feedback controller. PD: Photo-detector, LPF: Low pass filter.

Fig. 4.5 shows the configuration of the feedback controller of the stabilizer. The signal from a detector had 10 GHz clock component due to the chirp that was generated from the phase modulator. Without this chirp, the demodulated RZ-BPSK signal using homodyne detection does not have any clock component. This 10 GHz clock component from chirp depends on the phase relation between the optical carrier of the data signal and the local oscillator. The clock component was down converted to 1 MHz, rectified and then sent through the low pass filter.

84

This signal was used as an error signal for a PI (proportional-integral) controller. This does not require any pilot tone or dithering signal or decision circuit for feedback control.

4.3.3 Principle of Operation

Assume the electric field of the CW local oscillator is

$$E_{LO}(t) = E_o\, e^{i(\omega t + \phi_o + \phi_n(t))}, \tag{4.12}$$

where ϕ_0 is the initial phase and $\phi_n(t)$ is the phase noise of the laser. Then the electric field of the optical signal can be written as

$$E_d(t) = E_{do}(t)e^{i(\omega t + \phi_o + \phi_d(t) + \phi_n(t) + \phi_f)}, \tag{4.13}$$

where ϕ_d is the phase of data and ϕ_f is a static phase that is determined by the setting level of the feedback loop for stabilization. It is assumed that the optical paths of the data and local oscillator are well matched compared that they have the same phase noise from the laser source.

The output currents of **I** and **Q** channel from the 90° optical hybrid are

$$i_{I0}(t) = 4R\sqrt{P_{LO}P_d(t)}\,cos(\phi_d(t) + \phi_f)$$

$$\tag{4.14}$$

$$i_{Q0}(t) = 4R\sqrt{P_{LO}P_d(t)}\,sin(\phi_d(t) + \phi_f),$$

where P: *power*, R :*responsivity*

85

The static phase, ϕ_f, can be removed in software domain. The signal power, $P_d(t)$, and the data phase, $\phi_d(t)$, can be determined from these measured signals since the local oscillator power and the responsivity are known. $P_d(t)$ and $\phi_d(t)$ were re-sampled with the bit rate in software domain for the constellation diagram. When the chirp of the optical data is in the range of the measurement bandwidth, the chirp can be found from the time derivative of the measured phase.

4.3.4. Experimental Results

(a)   (b)
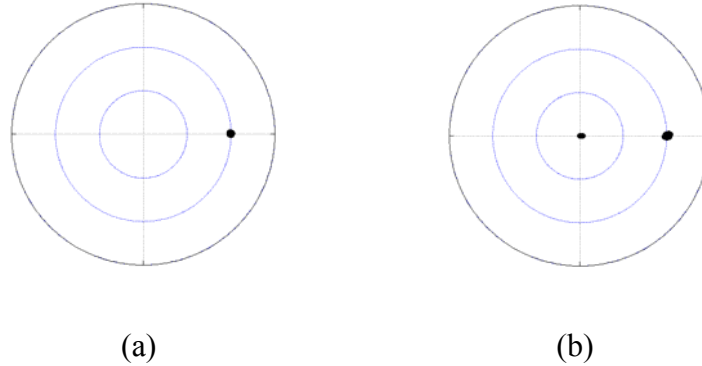
Fig. 4.6. Measured constellation diagrams. (a) RZ pulse train and (b) RZ data

The RZ pulse train without data was measured to test the accuracy of the measurement system. The RZ pulse train does not have any pattern dependent phase signal because it is driven by the clock signal. The measured constellation diagram is shown at Fig. 4.6(a). The radial axis is proportional to the optical intensity. The measured standard deviation of the phase was 0.4^o and

the peak-to-peak deviation was 2.4$^{\text{o}}$. The electrical signal to noise ratio (SNR) of measured intensity was 42 dB. The RZ data was used for the measurement to introduce pattern effect. The result is shown on the Fig. 4.6(b). The measured standard deviation of the data '1' was about 0.7$^{\text{o}}$ and the peak-to-peak deviation was 3.4$^{\text{o}}$. The measurement accuracy was good enough for the characterization considering 10$^{\text{o}}$ of standard deviation introduce 1 dB penalty for 10^{-10} BER in BPSK system.

Fig. 4.7(a) shows the measured constellation diagram of the RZ-BPSK signal. The phase noise for the two states were different because the driving signal had different noises for '0' and 'π', which was verified by observing driving electrical signal. The measured SNR was quite similar to that of the RZ data which was generated by an amplitude modulator, however, the measured phase noise for a state was much larger for this case. The phase noise and the amplitude noise were added intentionally to measure the constellation diagram with deterministic noise. Fig. 4.7(b) shows results for only phase noise added. The measured phase was spread but the intensity was not affected as expected. Fig. 4.7(c) shows the results when only amplitude noise was added. Fig. 4.7(d) was the case when the amplitude and phase noise were added at the same time. The measured constellation diagram shows the spread of the phase and the intensity comparing to the case of Fig. 4.7(a).
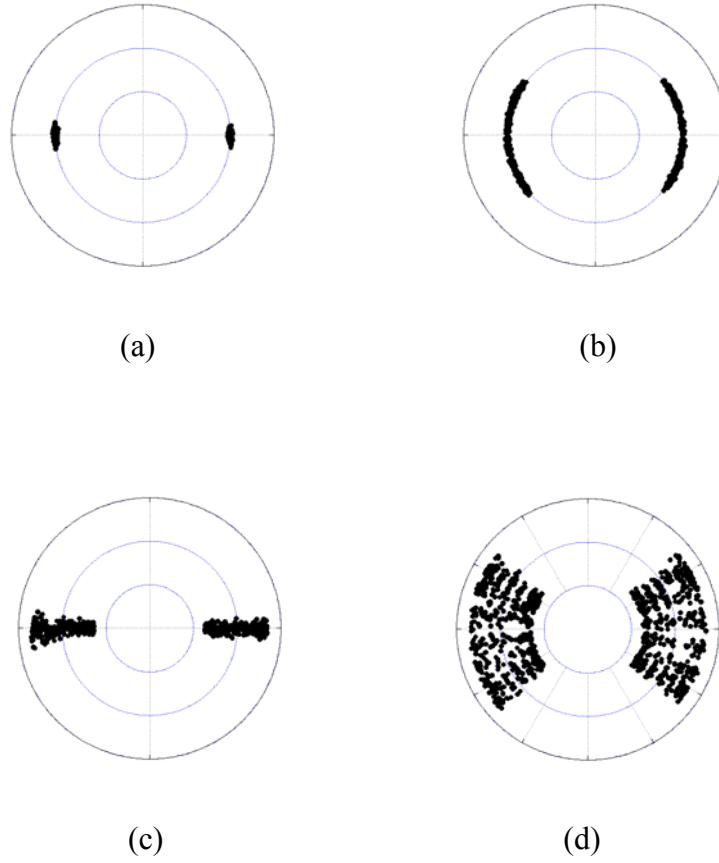
Fig. 4.7. Measured constellation diagrams of 10-Gb/s RZ-BPSK signal. (a) Without added noise, (b) with added phase noise, (c) with added amplitude noise, and (c) with added phase noise and amplitude noise.

(a)   (b)

(c)
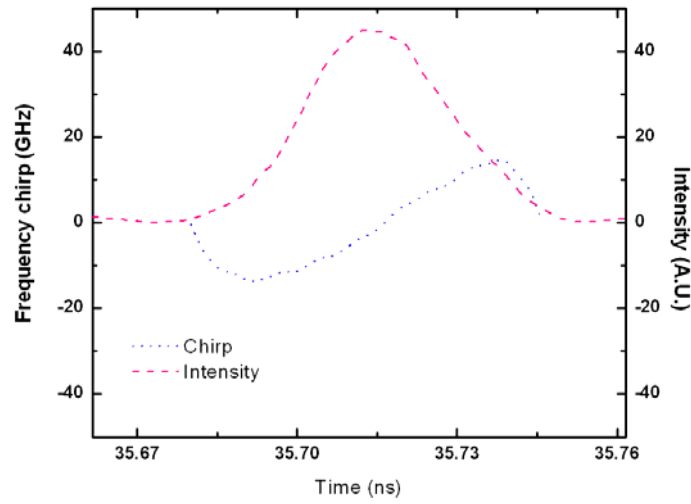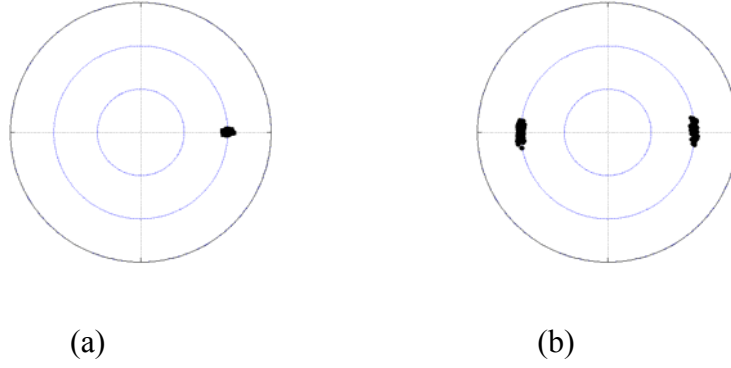
Fig. 4.8. (a) Measured constellation diagram of the RZ pulse train after transmission through 6 km of HNLF, (b) constellation diagram of the RZ-BPSK signal after transmission through 6 km of HNLF, and (c) the measured pulse profile and the chirp of the RZ-BPSK signal after transmission through 6 km of HNLF.

A piece of HNLF was added to signal path. The length of the HNLF was 6.058 km and the nonlinear coefficient was 9.75 km^{-1}W^{-1}. A similar length of standard single mode fiber was added to the local oscillator path to match the delay of the two optical paths (Fig. 4.4). An RZ pulse train was again used to test the measurement accuracy of the system. The measured constellation diagram of the RZ pulse train is shown on the Fig. 4.8(a). The measured standard deviation of the data was 0.8° and the peak-to-peak deviation was 4.5°. The power of the RZ pulse train was set to -3 dBm to avoid strong self-phase modulation. Fig. 4.8(b) shows the measured constellation of an RZ-BPSK signal transmitted through the HNLF. The result was comparable to the case of back-to-back in Fig. 4.7(a).

Fig. 4.8(c) shows the measured intensity profile (dashed line) and calculated profile of chirp (dotted line). The effective input power to the HNLF was about 16 dBm. The result shows the development of the chirp due to self-phase modulation of the RZ-BPSK signal. The measured chirp agrees with the expected amount from the given data.

4.3.5. Summary

Characterization of the 10-Gb/s RZ-BPSK signal was demonstrated using coherent detection technique. The measured optical intensity profile, chirp and constellation diagram were presented. A CW local oscillator was used and the electrical sampling was performed using a sampling scope. This can be a cost effective method compared to linear optical sampling systems using short optical sampling pulse trains when the bit rate and the frequency chirp of interest are in the electrical bandwidth of the measurement system. Carrier synchronization for coherent homodyne detection was achieved by monitoring 10-GHz clock component, which does not

require any pilot tone or dithering signal. This measurement technique can be used for characterization of the BPSK transmitter at transmission site.

CHAPTER FIVE: CONCLUSION

5.1. Summary of the work

All-optical timing synchronization (clock recovery) and all-optical carrier synchronization (carrier phase and polarization recover) were studied for future optical communications. Furthermore, linear optical sampling for characterization of advanced modulation formats, which will be employed in next generation optical communications, has been studied.

The dynamics and the limit of all-optical timing synchronization using MS-GC DFB (multi-section gain-coupled DFB) lasers have been studied. The fast lockup (~ 1ns) of all-optical clock recovery using MS-GC DFB lasers was well known. The new study of dynamics in simulation and experiment provided bases of getting long hold time (> 10 ns) and best phase stability of recovered clock. Quality of clock recovery affects the system performance. It was found that timing synchronization using MS-GC DFB laser can provide sufficient phase stability of the recovered clock with long hold time by limiting the bit-rate detuning. A record speed of 180 GHz for all-optical timing synchronization has been demonstrated using a MS-GC DFB laser. The MS-GC DFB laser exhibits self-pulsation over a continuous tuning range of more than 230 GHz, which enables all-optical timing synchronization at high bit rates. The ultrafast all-optical timing synchronization using MS-GC DFB laser can be used for future optical communications systems that have modulation speeds over 100 GHz.

All-optical carrier synchronization (carrier phase and polarization recovery) has been studied for advanced optical communications utilizing advanced modulation formats. Carrier synchronization is required for coherent detection, regeneration of PSK signal, and characterization of optical data. So far, there has been demonstration of carrier phase recovery

using decision-driven phase lock loop (DD-PLL) in real time. However, it required polarization alignment and the bandwidth of DD-PLL was small for practical purposes. We proposed, for the first time, an all-optical carrier synchronization scheme using a PSO, which adopted PSA as a gain block. All-optical carrier synchronization from 10-Gb/s BPSK data was demonstrated in experiment. This is a breakthrough in carrier synchronization, since it does not require any high bandwidth electronic feedback loop like DD-PLL and the carrier phase and polarization of the incoming data are tracked simultaneously in PSO.

The characterization of optical data generated by advanced modulation format requires carrier synchronization as well as timing synchronization. The timing synchronization provides the sampling bases in time domain. Carrier synchronization is a necessary component for coherent detection, which enable the measurement of the intensity and phase of data at the same time. Linear optical sampling is a strong candidate as a characterization tool for advanced optical communications in the future since it can measure the intensity and phase profile with high temporal resolution limited by the sampling pulsewidth. Study of requirements for the sampling source in coherent linear optical sampling showed the importance of carrier synchronization for reliable phase measurements. The phase measurement error is directly related to the quality of carrier synchronization.

Measurements of optical intensity profile, chirp and constellation diagram were demonstrated. A CW local oscillator was used instead of short sampling pulses and electrical sampling was performed using a sampling scope. This can be a cost effective method compared to linear optical sampling systems using short optical sampling pulse trains when the bit rate and the frequency chirp of interest are within the electrical bandwidth of the measurement system. A new feedback scheme, monitoring the 10-GHz clock component, was used to achieve carrier

93

synchronization for homodyne detection. The standard deviation of measured phase of RZ pulse train at the peaks was about 0.4° which showed excellent carrier phase synchronizations for measurement. This enabled the accurate characterization of the 10-Gb/s RZ-BPSK signal.

The study encompassed all-optical timing synchronization and carrier synchronization for advanced optical communications. In addition, coherent linear optical sampling was studied for characterization of optical data in advanced optical communications.

5.2 Future work

All-optical synchronizations are important for future optical communications as extensively discussed in this work. However, there is still research that needs to be done to improve the understanding of all-optical synchronizations and applications. The following is a list of future research and application topics.

♦ Dynamics and phase noise reduction

The dynamics of a PSO has not yet been studied. The signal build-up time in the oscillator will be determined by the loss, pumping power, and the length of the cavity. For the same loss factor and pumping power, longer cavities will give rise to longer build-up times. The lockup time of carrier synchronization (carrier recovery and polarization recovery) is directly related to this build-up time which can be important in practical applications for homodyne detection because it determines system latency.

Carrier synchronization with the PSO is expected to eliminate high frequency phase noise of the carrier because of the phase sensitive amplification process in the oscillator. The quality of the recovered carrier will affect the performance of application based on the recovered carrier,

such as all-optical DPSK regeneration. A detailed study of the quality of the recovered optical carrier is therefore required.

♦ PSO for WDM

In WDM systems utilizing advanced modulation formats, it is highly preferable to recover all the carrier phases and polarizations at the same time using a single PSO. This multi-channel carrier synchronization will reduce the system complexity and cost for coherent homodyne detection. The degenerate parametric oscillations will occur in the cavity when it is pumped with WDM BPSK data if the phase sensitive gain (based on degenerate four-wave mixing) is larger than phase insensitive gain (based on non-degenerate four-wave mixing). In this case, the optical carriers and phases in each channel will be recovered by PSO as shown in Fig. 5.1. However, further detailed study is required for practical implementation of the PSO for WDM.
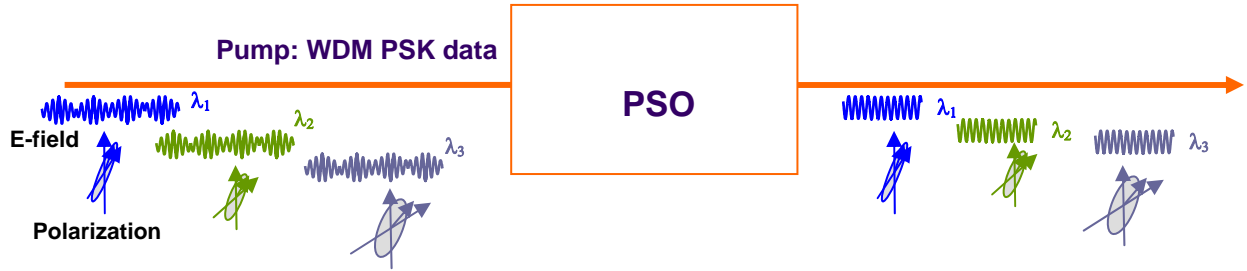
Fig. 5.1. Schematic diagram of simultaneous carrier synchronizations of each channel in WDM system

Fig. 5.2. Schematic diagram of coherent linear optical sampling at the receiver site.

♦ All-optical timing and carrier synchronizations

Ultrafast timing synchronization and all-optical carrier synchronization have been demonstrated separately so far. However, there was no proposed scheme of simultaneous all-optical timing and carrier synchronizations. Both timing and carrier synchronization are required for coherent detection and for full characterization of optical data at the receiver site. Timing synchronization provides the information of when to sample. Carrier synchronization is required for coherent homodyne detection. Fig. 5.2 shows the schematic diagram of measurement of the constellation diagram. First, carrier and clock signal are recovered from incoming data. The recovered optical carrier is modulated by the sub-clock of the recovered clock to generate short sampling pulse trains. The sampling pulse train can then be used for coherent linear optical sampling.

96

APPENDIX: INSTANTANEOUS FREQUENCY

A.1. Bandpass signal and Instantaneous frequency

A bandpass signal implies the existence of a reference frequency f_c around which the signal transform has a limited extent. The Fourier transform of a bandpass signal $x(t)$ is shown in Fig. A.1. To show the reference frequency explicitly, it is convenient to represent a bandpass function $x(t)$ in the following form:

$$x(t) = x_c(t)\cos 2\pi f_c t - x_s(t)\sin 2\pi f_c t , \qquad (A.1)$$

where f_c is the reference or carrier frequency. $x_c(t)$ is the in-phase modulation component and $x_s(t)$ is the quadrature modulation component of the baseband components of $x(t)$. The $x_c(t)$ and $x_s(t)$ are low pass functions so that the Fourier transforms of these functions will be between $-f_c$ and f_c.
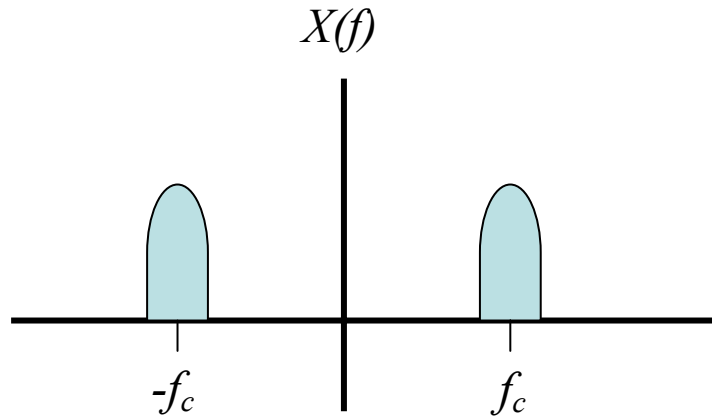
Fig. A. 1. $X(f)$: Fourier transform of a bandpass signal $x(t)$

Eq. (A.1) can be rewritten as the following form:

98

$$x(t) = a(t)\cos(2\pi f_c t + \phi(t)) , \qquad \qquad \text{(A.2)}$$

where

$$a(t) = [x_c^2(t) + x_s^2(t)]$$
$$\phi(t) = \tan^{-1}[x_s(t)/x_c(t)] \qquad \qquad \text{(A.3)}$$

$a(t)$ is the envelope and $\phi(t)$ is the phase modulation (or phase deviation). The frequency modulation (or deviation) $\xi(t)$ can be found from Eq. (A.3)

$$\xi(t) = \frac{1}{2\pi}\frac{d\phi(t)}{dt} = \frac{1}{2\pi}\phi'(t) = \frac{1}{2\pi}\frac{x_c(t)x_s'(t) - x_s(t)x_c'(t)}{x_c^2(t) + x_s^2(t)} , \qquad \qquad \text{(A.4)}$$

where the primes indicate time derivatives. Now we can define the instantaneous frequency of the bandpass signal $x(t)$ as

$$ins\,tan\,tan\,eous\,frequency = f_c + \xi(t) . \qquad \qquad \text{(A.5)}$$

The total instantaneous phase is the time integration of Eq. (A.5). The modulation components $x_c(t)$ and $x_s(t)$ can be calculated from a given bandpass signal $x(t)$ using Hilbert transform.

99

A. 2. Hilbert transform

We often need to know the relationships between the real and imaginary parts of a complex signal which is derived from a real signal. The relationships are generally described by the Hilbert transform. The Hilbert transform helps us relate the in-phase and quadrature-phase components but it is also used to create an analytic signal.

A real signal $x(t)$ can be written as

$$x(t) = \int_{-\infty}^{\infty} X(f) e^{i2\pi f t} df , \qquad (A.6)$$

where $X(f)$ is the Fourier transform of $x(t)$, which satisfies $X(f) = X^*(-f)$. Now let us think about a cosine wave $\cos(2\pi f_0 t)$ (in-phase component). The role of Hilbert transform is finding a sine wave (quadrature-phase component) from the cosine wave. The Fourier transform of the cosine wave is

$$X(f) = 0.5\delta(f + f_0) + 0.5\delta(f - f_0), \qquad (A.7)$$

which does not have any complex number because the cosine wave does not have any quadrature component (sine wave component). The Fourier transform of the sine wave can be found by multiplying $-i\,(=e^{-i\pi/2})$ for the positive spectral component and $i\,(=e^{i\pi/2})$ for the negative spectral component of the cosine wave. The Hilbert transform multiplies i for all negative frequency components of a signal and $-i$ for all positive frequency components. In other words,

all negative frequency components are phase shifted by 90° and all positive frequency components are shifted by -90°.

In time domain, the Hilbert transform is a convolution. The Hilbert transform of a real signal $x(t)$ is designated by $\hat{x}(t)$ defined as

$$\hat{x}(t) \equiv H[x(t)] \equiv x(t) * \frac{1}{\pi t} = -\frac{1}{\pi} \int_{-\infty}^{\infty} \frac{x(t+\tau)}{\tau} d\tau = \frac{1}{\pi} \int_{-\infty}^{\infty} \frac{x(t)}{t-\tau} d\tau . \qquad \text{(A.8)}$$

Fourier transform of the above equation is given as

$$\hat{X}(f) = F[\hat{x}(t)] = F[\frac{1}{\pi t}]X(f) = -i \operatorname{sgn}(f) X(f), \qquad \text{(A.9)}$$

where $\operatorname{sgn}(f)$ is 1 for positive frequencies, -1 for negative frequencies, and 0 for $f = 0$.

The properties of the Hilbert transform are

   a. It is a filter that changes the phase of the spectral components depending on the sign of their frequency.

   b. It only affects the phase of the signal. It has no effect on the amplitude.

   c. The signal and its Hilbert transform are orthogonal because the spectral components of the signal gain the phase shift by $\pm 90^o$ depend on the sign of the frequency.

   d. The signal and its Hilbert transform have identical energy because phase shift do not change the energy of the signal.
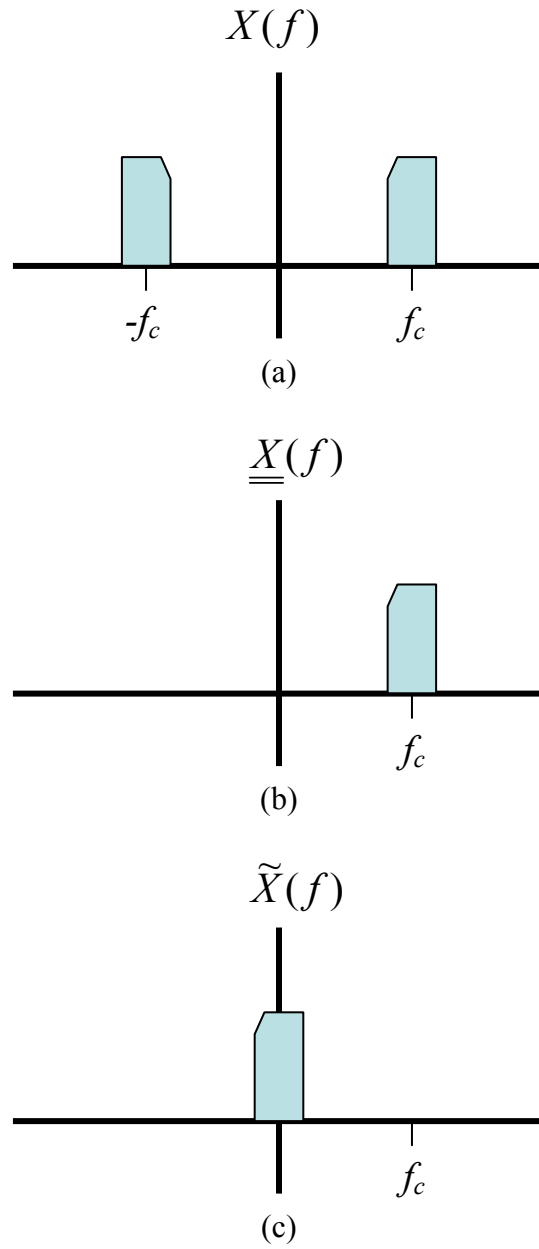
Fig. A. 2. (a) Fourier transform of a bandpass signal $x(t)$, (b) Fourier transform of the analytic signal $\underline{x}(t)$, (c) Fourier transform of the complex envelop $\tilde{x}(t)$.

A. 3. Analytic signal

The real signal $x(t)$ can be represented as the real part of a complex signal $\underline{x}(t)$, called the pre-envelope or analytic signal of $x(t)$, where

$$\underline{x}(t) = x(t) + i\hat{x}(t) = x(t) + iH[x(t)] \ .$$

(A.10)

The analytic signal, $\underline{x}(t)$, has a one-sided frequency function as shown on the following equations:

$$\underline{X}(f) = X(f) + iX(f) = X(f) + sgn(f)X(f)$$

(A.11)

$$\underline{X}(f) = \begin{cases} 2X(f), & f > 0 \\ X(f), & f = 0 \\ 0, & f < 0. \end{cases}$$

If we assume that the real signal $x(t)$ is a bandpass signal, we can find a reference frequency f_c such that the complex envelope $\tilde{x}(t)$ of the signal $x(t)$ is defined by

$$\tilde{x}(t) = \underline{x}(t)e^{-i2\pi f_c t} \, ,$$

(A.12)

or the Fourier transform of the complex envelope is

$$\tilde{X}(f) = \underline{X}(f + f_c).$$

(A.13)

The Fourier transforms associated with the bandpass real signal, analytic signal, and complex envelope are shown in Fig. A. 2.

The complex envelope $\tilde{x}(t)$ is related with the modulation components $x_c(t)$ and $x_s(t)$ as the following:

$$\tilde{x}(t) = x_c(t) + i\,x_s(t). \qquad\qquad (A.14)$$

This equation can be proved by comparing the analytic signal derived from Eq. (A.1) and (A.12).

Now, the instantaneous frequency can be found from Eqs. (A.4) and (A.5). For the calculation of instantaneous frequency of the real signal, any f_c that is larger than the bandwidth of modulation components and is in the bandpass signal can be chosen. The frequency of the maximum peak spectral component of the Fourier transform of the time-domain signal was chosen as f_c to calculate the instantaneous frequency in this thesis work.

REFERENCES

[1]   J. P. Turkiewicz, E. Tangdiongga, G. D. Khoe, and H. de Waardt, "Clock recovery and demultiplexing performance of 160-Gb/s OTDM field experiments," *IEEE Photonics Technology Letters*, vol. 16, pp. 1555-1557, 2004.

[2]   A. I. Siahlo, J. Seoane, A. T. Clausen, L. K. Oxenlowe, and P. Jeppensen, "320 Gb/s Single-polarization OTDM Transmission over 80 km Standard Transmission Fiber," *OFC 2005*, OFF3.

[3]   W. M. Mao, Y. H. Li, M. Al-Mumin, and G. F. Li, "All-optical clock recovery from RZ-format data by using a two-section gain-coupled DFB laser," *Journal of Lightwave Technology*, vol. 20, pp. 1705-1714, 2002.

[4]   O. Wada, "Ultrafast InP technologies for optical fiber communications," *OFC 2004, tutorial FD1*, http://www.ofcnfoec.org/materials/WadaFD1.pdf.

[5]   P. S. Cho, G. Harston, C. J. Kerr, A. S. Greenblatt, A. Kaplan, Y. Achiam, G. Levy-Yurista, M. Margalit, Y. Gross, and J. B. Khurgin, "Investigation of 2-b/s/Hz 40-Gb/s DWDM transmission over 4x100 km SMF-28 fiber using RZ-DQPSK and polarization multiplexing," *IEEE Photonics Technology Letters*, vol. 16, pp. 656-658, 2004.

[6]   C. Kim, G. Goldfarb, Y. Han, Z. H. Li, X. X. Li, and G. F. Li, "WDM transmission over 320 km EDFA-amplified SSMF using 30 Gb/s return-to-zero optical differential 8-level phase-shift keying (OD8PSK)," *Optics Express*, vol. 13, pp. 4044-4049, 2005.

[7]   S. Ferber, C. Schubert, R. Ludwig, C. Boerner, C. Schmidt-Langhorst, and H. G. Weber, "640 Gbit/s DQPSK, single wavelength-channel transmission over 480 km fibre link," *Electronics Letters*, vol. 41, pp. 1236-1237, 2005.

[8]   O. Leclerc, B. Lavigne, E. Balmefrezol, P. Brindel, L. Pierre, D. Rouvillain, and F. Seguineau, "Optical regeneration at 40 Gb/s and beyond," *Journal of Lightwave Technology*, vol. 21, pp. 2779-2790, 2003.

[9]   K. Croussore, I. Kim, Y. Han, C. Kim, G. F. Li, and S. Radic, "Demonstration of phase-regeneration of DPSK signals based on phase-sensitive amplification," *Optics Express*, vol. 13, pp. 3945-3950, 2005.

[10]   K. Croussore, I. Kim, C. Kim, Y. Han, and G. F. Li, "Phase-and-amplitude regeneration of differential phase-shift keyed signals using a phase-sensitive amplifier," *Optics Express*, vol. 14, pp. 2085-2094, 2006.

[11]   D. S. Ly-Gagnon, S. Tsukarnoto, K. Katoh, and K. Kikuchi, "Coherent detection of optical quadrature phase-shift keying signals with carrier phase estimation," *Journal of Lightwave Technology*, vol. 24, pp. 12-21, 2006.

[12]   C. Dorrer, C. R. Doerr, I. Kang, R. Ryfand, and L. Stulz, "High-sensitivity high-resolution sampling using linear optics and waveguide optical hybrid," *OFC 2004*, PDP18.

[13]   C. Dorrer, "Complete characterization of periodic optical sources by use of sampled test-plus-reference interferometry," *Optics Letters*, vol. 30, pp. 2022-2024, 2005.

[14]   C. Dorrer, C. R. Doerr, I. Kang, R. Ryf, J. Leuthold, and P. J. Winzer, "Measurement of eye diagrams and constellation diagrams of optical sources using linear optics and waveguide technology," *Journal of Lightwave Technology*, vol. 23, pp. 178-186, 2005.

[15] W. M. Mao, Y. H. Li, M. Al-Mumin, and G. F. Li, "All-optical clock recovery for both RZ and NRZ data," *IEEE Photonics Technology Letters*, vol. 14, pp. 873-875, 2002.

[16] C. Kim and G. Li, "Hybrid RZ to CSRZ format conversion," *Electronics Letters*, vol. 40, pp. 620-621, 2004.

[17] A. Miras-Legros, E. Legros, L. Giraudet, G. Wanlin, S. Vuye, and C. Joly, "Very high gain, high sensitivity, 40GHz narrowband photoreceiver for clock recovery," *Electronics Letters*, vol. 34, pp. 297-299, 1998.

[18] K. Murata and Y. Yamane, "40Gbit/s fully monolithic clock recovery IC using InAlAs/InGaAs/InP HEMTs," *Electronics Letters*, vol. 36, pp. 1617-1618, 2000.

[19] W. Mao, X. Wang, M. Al-Munin, and G. Li, "40 Gb/s all-optical clock recovery using three section self-pulsation DFB lasers," *OFC Proceedings 2000*, pp. 79-80.

[20] W. Mao and G. Li, "Ultrafast wavelength and polarization insensitive all-optical clock recovery," *OFC 2001*, MG3.

[21] G. Li, Y. Li, and W. Mao, "All-optical clock recovery using self-pulsing two-section gain-coupled DFB lasers," *IEEE/LEOS summer topicals 2002*, TuO2-31 – TuO2-32.

[22] B. Sartorius, S. Bauer, C. Bornoldt, M. Möhrle, H.-P. Nolting, and J. Slovak, "All-optical clock recovery for signal processing and regeneration," *IEEE/LEOS summer topicals*, 2002.

[23] Y. H. Li, C. Kim, G. F. Li, Y. Kaneko, R. L. Jungennan, and O. Buccafusca, "Wavelength and polarization insensitive all-optical clock recovery from 96-Gb/s data by using a two-section gain-coupled DFB laser," *IEEE Photonics Technology Letters*, vol. 15, pp. 590-592, 2003.

[24] S. Arahira, S. Sasaki, K. Tachibana, and Y. Ogawa, "All-optical 160-Gb/s clock extraction with a mode-locked laser diode module," *IEEE Photonics Technology Letters*, vol. 16, pp. 1558-1560, 2004.

[25] M. W. Chbat, P. A. Perrier, and P. R. Prucnal, "Optical Clock Recovery Demonstration Using Periodic Oscillations of a Hybrid Electrooptic Bistable System," *IEEE Photonics Technology Letters*, vol. 3, pp. 65-67, 1991.

[26] X. S. Yao and G. Lutes, "A high-speed photonic clock and carrier recovery device," *IEEE Photonics Technology Letters*, vol. 8, pp. 688-690, 1996.

[27] X. H. Wang, W. M. Mao, M. Al-Mumin, S. A. Pappert, J. Hong, and G. F. Li, "Optical generation of microwave/millimeter-wave signals using two-section gain-coupled DFB lasers," *IEEE Photonics Technology Letters*, vol. 11, pp. 1292-1294, 1999.

[28] B. Sartorius, M. Mohrle, and U. Feiste, "12-64 Ghz Continuous Frequency Tuning in Self-Pulsating 1.55-Mu-M Multi-Quantum-Well Dfb Lasers," *IEEE Journal of Selected Topics in Quantum Electronics*, vol. 1, pp. 535-538, 1995.

[29] I. Kim, C. Kim, G. F. Li, P. L. Wa, and J. Hong, "180-GHz clock recovery using a multisection gain-coupled distributed feedback laser," *IEEE Photonics Technology Letters*, vol. 17, pp. 1295-1297, 2005.

[30] M. Al-Mumin, X. H. Wang, W. M. Mao, S. A. Pappert, and G. F. Li, "Optical generation and sideband injection locking of tunable 11-120GHz microwave/millimetre signals," *Electronics Letters*, vol. 36, pp. 1547-1548, 2000.

[31] I. Kim, C. Kim, P. L. LiKamWa, and G. Li, "Dynamics of All-Optical Clock Recovery Using Two-Section Index- and Gain-Coupled DFB Lasers," *Journal of Lightwave Technology*, vol. 23, pp. 1704-1711, 2005.

[32]   S. Norimatsu, K.Iwashita, and K. Noguchi, "An 8 Gb/s QPSK optical homodyne detection experiment using external-cavity laser diodes," *IEEE Photonics Technology Letters*, vol. 4, pp. 765 - 767 1992.

[33]   L. G. Kazovsky, "Decision-Driven Phase-Locked Loop for Optical Homodyne Receivers: Performance Analysis and Laser Linewidth Rquirements," *Journal of Lightwave Technology*, vol. 3, pp. 1238-1247, 1985.

[34]   R. Noe, "Phase noise tolerant synchronous QPSK receiver concept with digital I&Q baseband processing," *in Proc. Opto-Electronics and Communications Conf. (OECC) 2004*, Japan, pp. 818-819.

[35]   S. Kawanishi, T. Yamamoto, M. Nakazawa, and M. M. Fejer, "High sensitivity waveform measurement with optical sampling using quasi-phasematched mixing in LiNBO3 waveguide," *Electronics Letters*, vol. 37, pp. 842-844, 2001.

[36]   C. Dorrer, J. Leuthold, and C. R. Doerr, "Direct measurement of constellation diagrams of optical sources," *OFC 2004*, PDP33.

[37]   L. G. Kazovsky, "Balanced Phase-Locked Loops for Optical Homodyne Receivers - Performance Analysis, Design Considerations, and Laser Linewidth Requirements," *Journal of Lightwave Technology*, vol. 4, pp. 182-195, 1986.

[38]   F. Herzog, K. Kudielka, D. Erni, and W. Bächtold, "Optical phase locked loop for transparent inter-satellite communications," *Optics Express*, vol. 13, pp. 3816-3821, 2005.

[39]   X. H. Wang, G. F. Li, J. Hong, and S. A. Pappert, "Spatiotemporal dynamics and high-frequency self-pulsations in two-section distributed feedback lasers," *Journal of the Optical Society of America B-Optical Physics*, vol. 16, pp. 2030-2039, 1999.

[40]   S. Nakamura, Y. Ueno, and K. Tajima, "168-Gb/s All-Optical Wavelength Coversion With a Symmetric-Mach-Zehnder-Type Switch," *IEEE Photonics Technology Letters*, vol. 13, pp. 1091-1093, 2001.

[41]   L. M. Zhang, S. F. Yu, M. C. Nowell, D. D. Marcenac, J. E. Carroll, and R. G. S. Plumb, "Dynamic Analysis of Radiation and Side-Mode Suppression in a 2nd-Order DFB Laser Using Time-Domain Large-Signal Traveling-Wave Model," *IEEE Journal of Quantum Electronics*, vol. 30, pp. 1389-1395, 1994.

[42]   H. Wenzel and U. Bandelow, "Self pulsations by mode degeneracy in two-section DFB lasers," *SPIE Proc. Vol. 2399*, pp. 195-206, 1995.

[43]   W. Mao, *High speed all-optical clock recovery and 3R regeneration, Ph. D. dissertation thesis, University of Central Florida*, 2001.

[44]   K. Sato, S. Kuwahara, Y. Miyamoto, K. Murata, and H. Miyazawa, "Mode-locked lasers for 43-Gb/s carrier-suppressed return-to-zero pulse generation," *in Proc. ECOC'01*, pp. 340-341, 2001.

[45]   R. Lang, "Injection Locking Properties of a Semiconductor-Laser," *IEEE Journal of Quantum Electronics*, vol. 18, pp. 976-983, 1982.

[46]   F. Mogensen, H. Olesen, and G. Jacobsen, "Locking Conditions and Stability Properties for a Semiconductor-Laser with External Light Injection," *IEEE Journal of Quantum Electronics*, vol. 21, pp. 784-793, 1985.

[47]   I. Petitbon, P. Gallion, G. Debarge, and C. Chabran, "Locking Bandwidth and Relaxation Oscillations of an Injection-Locked Semiconductor-Laser," *IEEE Journal of Quantum Electronics*, vol. 24, pp. 148-154, 1988.

[48] R. Q. Hui, "Optical Psk Modulation Using Injection-Locked Dfb Semiconductor-Lasers," *IEEE Photonics Technology Letters*, vol. 2, pp. 743-746, 1990.

[49] A. Vizzino, M. Gioannini, and N. Montrosset, "Dynamic simulation of clock recovery with self-pulsating three-section distributed-feedback lasers," *IEEE Journal of Quantum Electronics*, vol. 38, pp. 1580-1586, 2002.

[50] H. Urkowitz, *Signal theory and random processes, Norwood, MA: Artech House* 1983, pp.65-76.

[51] P. Rees, P. McEvoy, A. Valle, J. O'Gorman, S. Lynch, P. Landais, L. Pesquera, and J. Hegarty, "A theoretical analysis of optical clock extraction using a self-pulsating laser diode," *IEEE Journal of Quantum Electronics*, vol. 35, pp. 221-227, 1999.

[52] C. A. Eldering, F. Herreriasmartin, R. Martingomez, and P. J. Garciaarribas, "Digital Burst Mode Clock Recovery Technique for Fiberoptic Systems," *Journal of Lightwave Technology*, vol. 12, pp. 271-279, 1994.

[53] H. Dong, H. Z. Sun, G. H. Zhu, Q. Wang, and N. K. Dutta, "Clock recovery using cascaded $LiNbO_3$ modulator," *Optics Express*, vol. 12, pp. 4751-4757, 2004.

[54] H. F. Chou, Z. Y. Hu, J. E. Bowers, D. J. Blumenthal, K. Nishimura, R. Inohara, and M. Usami, "Simultaneous 160-Gb/s demultiplexing and clock recovery by utilizing microwave harmonic frequencies in a traveling-wave electroabsorption modulator," *IEEE Photonics Technology Letters*, vol. 16, pp. 608-610, 2004.

[55] T. Ohno, K. Sato, R. Iga, Y. Kondo, I. Ito, T. Furuta, K. Yoshino, and H. Ito, "Recovery of 160 GHz optical clock from 160 Gbit/s data stream using modelocked laser diode," *Electronics Letters*, vol. 40, pp. 265-267, 2004.

[56] S. Akiba, K. Utaka, K. Sakai, and Y. Matsushima, "Temperature Dependence of Lasing Characteristics of InGaAsP/InP Distributed Feedback Lasers in 1.5 μm Range," *Jpn. J. Appl. Phys.*, vol. 21, pp. 1736-1740, 1982.

[57] K. Croussore, C. Kim, and G. F. Li, "All-optical regeneration of differential phase-shift keying signals based on phase-sensitive amplification," *Optics Letters*, vol. 29, pp. 2357-2359, 2004.

[58] http://monet.unibas.ch/~elmer/pendulum/bif.htm.

[59] M. H. Chou, I. Brener, G. Lenz, R. Scotti, E. E. Chaban, J. Shmulovich, D. Philen, S. Kosinski, K. R. Parameswaran, and M. M. Fejer, "Efficient wide-band and tunable midspan spectral inverter using cascaded nonlinearities in LiNbO3 waveguides," *IEEE Photonics Technology Letters*, vol. 12, pp. 82-84, 2000.

[60] S. Diez, R. Ludwig, C. Schmidt, U. Feiste, and H. G. Weber, "160-Gb/s optical sampling by gain-transparent four-wave mixing in a semiconductor optical amplifier," *IEEE Photonics Technology Letters*, vol. 11, pp. 1402-1404, 1999.

[61] J. Li, J. Hansryd, P. O. Hedekvist, P. A. Andrekson, and S. N. Knudsen, "300-Gb/s eye-diagram measurement by optical sampling using fiber-based parametric amplification," *IEEE Photonics Technology Letters*, vol. 13, pp. 987-989, 2001.

[62] S. Nogiwa, H. Ohta, Y. Kawaguchi, and Y. Endo, "Improvement of sensitivity in optical sampling system," *Electronics Letters*, vol. 35, pp. 917-918, 1999.

[63] J. Li, M. Westlund, H. Sunnerud, B. E. Olsson, M. Karlsson, and P. A. Andrekson, "0.5-Tb/s eye-diagram measurement by optical sampling using XPM-induced wavelength shifting in highly nonlinear fiber," *IEEE Photonics Technology Letters*, vol. 16, pp. 566-568, 2004.

[64]   A. H. Gnauck, S. Chandrasekhar, J. Leuthold, and L. Stulz, "Demonstration of 42.7-Gb/s DPSK receiver with 45 photons/bit sensitivity," *IEEE Photonics Technology Letters*, vol. 15, pp. 99-101, 2003.

[65]   C. Dorrer, "Direct measurement of nonlinear coefficient of optical fibre using linear optical sampling," *Electronics Letters*, vol. 41, pp. 8-10, 2005.

[66]   S. T. Cundiff, "Phase stabilization of ultrashort optical pulses," *Journal of Physics D-Applied Physics*, vol. 35, pp. R43-R59, 2002.

[67]   A. Takada and W. Imajuku, "Linewidth narrowing and optical phase control of mode-locked semiconductor ring laser employing optical injection locking," *IEEE Photonics Technology Letters*, vol. 9, pp. 1328-1330, 1997.

[68]   I. Kim, C. Kim, and G. F. Li, "Requirements for the sampling source in coherent linear sampling," *Optics Express*, vol. 12, pp. 2723-2730, 2004.

[69]   P. B. Gallion and G. DeBarge, "Quantum Phase Noise and Field Correlation in Single Frequency Semiconductor Laser Systems," *IEEE Journal of Quantum Electronics*, vol. 20, pp. 343-349, 1984.